REPORT DOCUMENTATION PAGE

JAN AFRL-SR-AR-TR-03-

0014

Public reporting burden for this collection of information is estimated to average 1 hour per response, including the time for reviewing instruc
data needed, and completing and reviewing this collection of information. Send comments regarding this burden estimate or any other aspe
this burden to Department of Defense, Washington Headquarters Services, Directorate for Information Operations and Reports (0704-0188)
4302. Respondents should be aware that notwithstanding any other provision of law, no person shall be subject to any penalty for failing to
valid OMB control number. **PLEASE DO NOT RETURN YOUR FORM TO THE ABOVE ADDRESS.**

1. REPORT DATE (DD-MM-YYYY) 14/01/2003	2. REPORT TYPE Final	3. DATES COVERED (From - To) 01/2000 to 09/2002

4. TITLE AND SUBTITLE

Large Eddy Simulation of Complex Flows: Wall Modeling
Techniques for Large-Eddy Simulation

5a. CONTRACT NUMBER

5b. GRANT NUMBER
AF F9620-00-1-0111

5c. PROGRAM ELEMENT NUMBER

6. AUTHOR(S)

Parviz Moin, Jeremy Templeton, Meng Wang, Franck Nicoud and Jeffrey Baggett

5d. PROJECT NUMBER

5e. TASK NUMBER

5f. WORK UNIT NUMBER

7. PERFORMING ORGANIZATION NAME(S) AND ADDRESS(ES)

Stanford University
Mechanical Engineering
Building 500, Room 500C
Stanford, CA 94305-3035

8. PERFORMING ORGANIZATION REPORT NUMBER

SPO 23089

9. SPONSORING / MONITORING AGENCY NAME(S) AND ADDRESS(ES)
Dr. Thomas Beutner
AFOSR/NA
801 North Randolph St., Rm.
Arlington, VA 22203-1977

10. SPONSOR/MONITOR'S ACRONYM(S)

11. SPONSOR/MONITOR'S REPORT NUMBER(S)

12. DISTRIBUTION / AVAILABILITY STATEMENT

Approved for public release. Distribution is unlimited.

20030211 131

13. SUPPLEMENTARY NOTES

14. ABSTRACT

In the LES of high Reynolds number wall-bounded flows, wall modeling is needed to alleviate the severe near-wall
resolution requirement. Simple algebraic models such as the instantaneous log-law are inadequate for predicting
complex flows with strong pressure gradients and separation. We have explored two classes of wall models: those
based on the turbulent boundary-layer (TBL) equations and those based on control theory. Recent application of the
TBL equation model to LES of the flow over a cylinder at super-critical Reynolds number is discussed. The emphasis
of the report is on control based wall modeling, in which sub-optimal control strategy is used to find the wall
stresses that will force the outer LES toward a target profile. Results from channel-flow simulation indicate that
in order to obtain the correct mean velocity profile (the log law), the wall stresses must not only model the
physics but also compensate for numerical and SGS modeling errors. The data generated by this sub-optimal control
strategy are then used to derive a linear stochastic estimate model. The mathematical formulation and issues of key
importance in control-based wall modeling are detailed. Efforts towards a predictive and inexpensive wall model in
the control framework are detailed.

15. SUBJECT TERMS
Large-Eddy Simulation, channel flow, turbulence, wall models, control theory, high Reynolds-number flow, sub-
optimal control, turbulent boundary-layer equations.

16. SECURITY CLASSIFICATION OF: Unclassified			17. LIMITATION OF ABSTRACT	18. NUMBER OF PAGES	19a. NAME OF RESPONSIBLE PERSON Parviz Moin
a. REPORT Unclassified	**b. ABSTRACT** Unclassified	**c. THIS PAGE** Unclassified	None	47	**19b. TELEPHONE NUMBER** (include area code) (650) 723-9713

Standard Form 298 (Rev. 8-98)
Prescribed by ANSI Std. Z39.18

Wall Modeling Techniques for Large-Eddy Simulation

Parviz Moin, Jeremy Templeton, Meng Wang,
Franck Nicoud, and Jeffrey Baggett

Abstract

In the large-eddy simulation (LES) of high Reynolds number wall-bounded flows, wall modeling is needed to alleviate the severe near-wall resolution requirement. Simple algebraic models such as the instantaneous log-law are inadequate for predicting complex flows with strong pressure gradients and separation. Under the sponsorship of AFOSR, we have explored two classes of wall models: those based on the turbulent boundary-layer (TBL) equations and those based on control theory. In this report, a recent application of the TBL equation model to LES of the flow over a cylinder at super-critical Reynolds number will first be discussed. The emphasis of the report is, however, on control based wall modeling, in which sub-optimal control strategy is used to find the wall stresses that will force the outer LES toward a target profile. Results from channel-flow simulation indicate that in order to obtain the correct mean velocity profile (the log law), the wall stresses must not only model the physics but also compensate for numerical and SGS modeling errors. The data generated by this sub-optimal control strategy are then used to derive a linear stochastic estimate model. The mathematical formulation and issues of key importance in control-based wall modeling will be discussed in detail. Current efforts towards a predictive and inexpensive wall model in the control framework will also be presented.

Wall Modeling Techniques for Large-Eddy Simulation

Parviz Moin, Jeremy Templeton, Meng Wang,
Franck Nicoud, and Jeffrey Baggett

Stanford University
Mechanical Engineering Department
Flow Physics and Computation Division
Stanford, CA 94305-3030

Chapter 1

Introduction

Large-eddy simulations (LES) of high Reynolds number flows are difficult to perform due to the need to include a large number of grid points in the near wall region. While LES models the small scales of the flow and resolves the large, dynamically important scales, near the wall, eddies scale with the distance from the wall and move increasingly closer to the wall as the Reynolds number increases. These eddies are dynamically important despite their size. Unfortunately, the eddy viscosity sub-grid scale (SGS) models only make a small contribution to the total Reynolds stress. This makes these models invalid near the wall [21], unless the LES grid is sufficiently refined to resolve the near-wall vortical structures. The required number of grid points for such a wall-resolved LES scales as Re_τ^2 in an attached boundary layer [4], which is only a slight improvement on the scaling for a full direct numerical simulation (DNS) of $Re^{9/4}$.

The technique of wall modeling was developed to reduce the Reynolds number scaling of LES resolution, so that LES could be applied in practical situations. For recent reviews, see [13] and [35]. The approach has a long history dating back to the atmospheric science and oceanographic applications. Limited by the computational power of the time, Deardorff [16] was the first to implement a model for the wall layer in an LES of a channel flow at infinite Reynolds number. He imposed constraints on wall-parallel velocities in terms of their wall-normal second derivatives to ensure the LES satisfied the log-law in mean. The wall transpiration velocity was set to zero. The first "modern" wall model was developed by Schumann [37]. It is a modern wall model in the sense that the wall stresses were determined directly by an algebraic model. The wall stresses were found by assuming that they were in phase with the velocity at the first off-wall grid point and that the deviation from their mean was proportional to the deviation of the velocity from its mean. Since the flow was in a channel, both the mean wall stresses and mean velocities were known. The transpiration velocity, as in the case of Deardorff [16], was set to zero.

Many improvements to this basic model have been made in the intervening years. For example, Piomelli *et al.* [36] added an offset to the velocity to account for the inclination of the eddies to obtain:

$$
\begin{aligned}
\tau_{12}^w(x,z) &= \frac{u(x+\Delta_s, y_1, z)}{\langle u \rangle} \langle \tau_w \rangle, \\
V(x,0,z) &= 0, \\
\tau_{32}^w(x,z) &= \frac{w(x+\Delta_s, y_1, z)}{\langle u \rangle} \langle \tau_w \rangle,
\end{aligned}
\tag{1.1}
$$

where Δ_s is an empirical displacement related to the mean orientation of vortical structures near the wall, y_1 is the wall-normal coordinate of the first off-wall grid points, and $\langle \cdot \rangle$ denotes averaging in the wall-parallel (x-z) plane. For atmospheric boundary layers, Mason & Callen [27] enforces an

instantaneous logarithmic law in each grid cell adjacent to the wall. Other efforts include those by Grötzbach [18], Werner & Wengle [44], and Hoffman & Benocci [20]. While these types of algebraic models produced reasonable results in the LES of plane channels and annuli, they are in general inadequate for flows in more complex geometries. In these flows, adverse pressure gradients and separated regions are common, and methods based on an equilibrium balance of stresses and a logarithmic velocity profile give inaccurate results.

To address this robustness issue in wall modeling, several investigators used more elaborate near-wall flow models to compute the wall stresses (see e.g. [8] and [13]). This type of approach divides the computational domain into two regions: one near the wall and one away from the wall. A simplified set of equations based on turbulent boundary-layer (TBL) approximations are solved on a near wall grid separate from the outer LES grid, subject to boundary conditions determined from the outer LES velocity together with the no-slip wall. The equations solved in the wall-layer are of the following general form,

$$\frac{\partial}{\partial y}\left[(\nu + \nu_t)\frac{\partial u_i}{\partial y}\right] = \frac{1}{\rho}\frac{\partial p}{\partial x_i} + \frac{\partial u_i}{\partial t} + \frac{\partial}{\partial x_j}u_i u_j, \quad i = 1, 3, \tag{1.2}$$

although simplified versions, with the right hand side set to zero or the pressure gradient alone, have also been considered [13, 42]. In Eq. (1.2) ν_t is given by a RANS eddy viscosity model, and the pressure is imposed from the LES solution and assumed constant across the wall layer. The computed wall stress is then provided to the LES as a boundary condition. While this method does require the solution of an extra set of equations, the simplifications made in these equations makes its cost much less than the evaluation of the LES equations. This method was tested in a plane channel, square duct, and rotating channel by Balaras *et al.* [8] and in a plane channel and backward-facing step by Cabot & Moin [13]. More recently, Wang & Moin [42] used this method with a dynamically adjusted RANS eddy viscosity to perform an LES of an airfoil trailing edge flow [41] with incipient separation. The results are better than those of the algebraic models, since the TBL equations can account for more of the physics of the flow. Nonetheless, there is insufficient evidence of robustness of this approach, particularly on coarse meshes and at very high Reynolds numbers.

To further assess the accuracy of this approach for high Reynolds number flows under coarse mesh resolution, a more severe test case of the flow over a cylinder at supercritical Reynolds number has been considered. This is described in detail in Chapter 2. The results are mixed. While the method is capable of capturing correctly the delayed boundary-layer separation and reduced drag coefficients after the drag crisis, the Reynolds-number dependence of the drag coefficient has not been captured, and the solutions become increasingly inaccurate at higher Reynolds numbers. It is argued that at such marginal resolution, the SGS modeling errors and numerical errors tend to dominate the LES in the near-wall region, which cannot be corrected by a physical based wall model.

The difficulty of formulating a robust wall model was highlighted in [12]. In that work, a backward facing step LES was performed using the "exact" time series of the wall stress from a resolved LES as the wall model. The results of this approach were not satisfactory and in fact not an improvement over the other types of wall models previously mentioned. This indicates that SGS and numerical errors are playing an important role in the coarse grid LES, which have not been accounted for by the previous wall models. To investigate this hypothesis and determine what information a wall model must provide to the LES, we used optimal control techniques to compute the wall stresses in a channel LES at $Re_\tau = 4000$. This work is discussed in Chapter 3 (see also [33, 5]). A cost function is defined to be the difference between the plane-averaged LES streamwise and spanwise velocity fields and their known mean values (log-law in the streamwise

2

direction and zero in the spanwise direction). Adjoint equations are used to determine the cost function derivatives, and iterations are performed at each time step to determine the best wall stress. The simulation results confirm that, to obtain the correct mean velocity profile, the wall stresses must not only model the physics but also compensate for numerical and SGS modeling errors. The data generated by this suboptimal control strategy is then used to derive a linear stochastic estimate (LSE) model which predicts the wall stresses from the near-wall velocity field. When used in actual simulations, the LSE model is shown to yield accurate mean velocity profiles over a range of Reynolds numbers. However, it is found to be sensitive to the numerical method, SGS model, and grid employed.

While valuable insight has been gained from the above control-based wall modeling, the method is not useful as a predictive tool since a target velocity profile must be specified *a priori*. The computational cost for the sub-optimal control is very high since it requires both the solution of adjoint equations and many iterations to achieve convergence. Furthermore, the LSE models generated from such computations are too sensitive to the numerical parameters to construct a universal LSE coefficient database. To overcome these drawbacks, we have explored a low-cost modeling approach using techniques borrowed from optimal shape design [31] and a RANS model to formulate a feedback controller. The mathematical framework and some test results are presented in Chapter 4.

Chapter 2

Wall Modeling in High Reynolds Number Flow over a Cylinder

As mentioned in the previous chapter, wall models based on TBL equations and their simplified forms [8, 13, 42] have received much attention in recent years. These models, used with a RANS type of eddy viscosity, have shown promise for complex-flow predictions. The objective of this chapter is to further assess the viability and accuracy of this technique for high Reynolds number complex wall-bounded flows.

The flow around a circular cylinder represents a canonical problem for validating new approaches in computational fluid dynamics. It is therefore reasonable or even necessary to subject the LES wall modeling methodology to the same "grand challenge". To take the best advantage of wall modeling, we concentrate on the super-critical flow regime in which the boundary layer on the cylinder becomes turbulent prior to separation. This is, to our knowledge, the first such attempt using LES, although a related method known as detached-eddy simulation (DES), in which the entire attached boundary layer is modeled, has been tested in this type of flow [39]. Breuer [11] recently conducted an LES study at a high sub-critical Reynolds number of $Re_D = 1.4 \times 10^5$, and showed fairly good comparison with experimental data in the near wake. In the present work, three simulations, at $Re_D = 5 \times 10^5$, 1×10^6, and 2×10^6, have been performed. Simulation results and comparisons with experimental data are summarized below.

2.1 Numerical method and procedure

The same LES code and wall model implementation as used in [42] are used for the present calculations. The energy-conservative numerical scheme is of hybrid finite-difference/spectral type, written for a C-mesh [28]. The time advancement is achieved by the fractional-step method, in combination with the Crank-Nicolson method for viscous terms and third-order Runge-Kutta scheme for convective terms. A multi-grid iterative procedure is used to solve the Poisson equation for pressure. The SGS stress tensor is modeled using the dynamic SGS model [17, 25].

The computational domain has a spanwise size of $2D$ (D = cylinder diameter), over which the flow is assumed periodic and 48 grid points are distributed uniformly. In the planes perpendicular to the span, 401×120 grid points are used in the C-mesh, extending approximately $22D$ upstream of the cylinder, $17D$ downstream of the cylinder, and $24D$ into the far-field. Potential-flow solutions are imposed as boundary conditions in the far-field, and convective boundary conditions are used at the outflow boundary. Running at a maximum CFL number of 1.5, the non-dimensional time step $\Delta t U_\infty / D$ typically varies between 0.0030 and 0.0045. To obtain the results presented here,
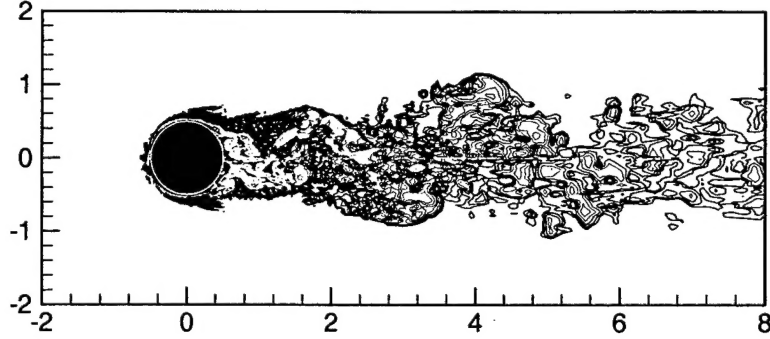
Figure 2.1: Instantaneous vorticity magnitude at a given spanwise cut for flow over a circular cylinder at $Re_D = 10^6$. 25 contour levels from $\omega D/U_\infty = 1$ to $\omega D/U_\infty = 575$ (exponential distribution) are plotted.

the simulations have advanced at least 150 dimensionless time units. The statistics are collected over the last 75 or so time units.

Approximate boundary conditions on the cylinder surface are imposed in terms of wall shear stress estimated from a wall model of the form

$$\frac{\partial}{\partial y}\left[(\nu + \nu_t)\frac{\partial u_i}{\partial y}\right] = \frac{1}{\rho}\frac{\partial p}{\partial x_i}, \qquad i = 1,3 \tag{2.1}$$

This is a simpler variant of the TBL equation model (cf. Eq. (1.2)) which allows for easier implementation and lower computational cost. Although Wang & Moin have shown [42] that the full TBL equations (with dynamically adjusted ν_t) give better results in their trailing-edge flow, the discrepancy may be partly related to a surface curvature discontinuity which is absent from the cylinder surface. Since the pressure is taken from the LES at the edge of the wall layer, Eq. (2.1) can be integrated to the wall to obtain a closed-form solution for the wall shear stress components [42]

$$\tau_{wi} = \frac{\rho}{\int_0^\delta \frac{dy}{\nu+\nu_t}}\left\{u_{\delta_i} - \frac{1}{\rho}\frac{\partial p}{\partial x_i}\int_0^\delta \frac{ydy}{\nu+\nu_t}\right\}, \tag{2.2}$$

where $u_{\delta i}$ denotes the tangential velocity components from LES at the first off-wall velocity nodes, at distance δ from the wall. In attached flows these nodes are generally placed within the lower edge of the logarithmic layer. In the present flow, however, δ^+ (in wall units) is found to vary from 0 to 100 depending on the local skin friction. The eddy viscosity is modeled by a damped mixing-length model: $\nu_t/\nu = \kappa y_w^+\left(1 - e^{-y_w^+/A}\right)^2$, where $y_w^+ = y_w u_\tau/\nu$ is the distance to the wall in wall units, $\kappa = 0.4$, and $A = 19$.

2.2 Results and discussion

In Figure 2.1, the contours of the vorticity magnitude at a given time instant and spanwise plane are plotted for $Re_D = 10^6$. Large coherent structures are visible in the wake, but they are not as well organized and periodic as in typical Kármán streets at lower (sub-critical) and higher (post-critical) Reynolds numbers. Compared to flows at lower Reynolds number (e.g. [23, 11]), the boundary-layer separation is much delayed and the wake is narrower, resulting in a much smaller
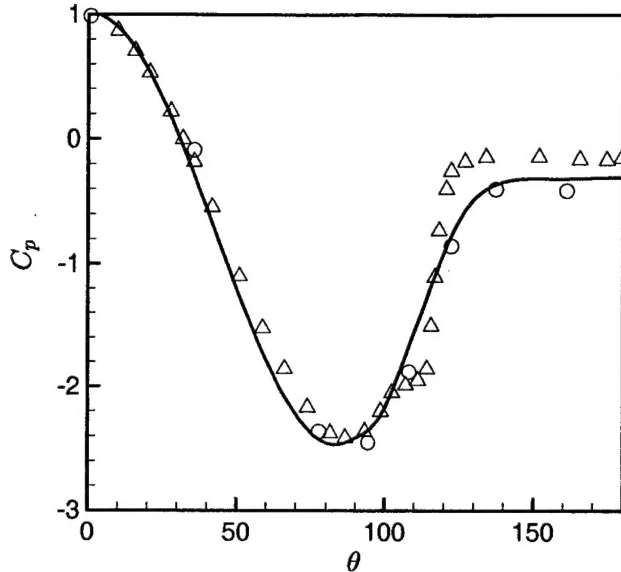
5

Figure 2.2: Mean pressure distribution on the circular cylinder. ——— , Present LES at $Re_D = 10^6$; ○ , Experiment of Warschauer & Leene [43] at $Re_D = 1.26 \times 10^6$ (spanwise averaged); △ , Experiment of Flachsbart (in [45]) at $Re_D = 6.7 \times 10^5$.

drag coefficient. Note that the rather thick layer seen along the cylinder surface consists mostly of vorticity contours of small magnitude. These levels are necessary for visualizing the wake structure, but are not representative of the boundary-layer thickness. The true boundary layer, with strong vorticity, is extremely thin in the attached region.

A comparison with two sets of experimental data of the mean pressure distribution on the cylinder surface is depicted in Figure 2.2. Very good agreement is observed between the LES at $Re_D = 10^6$ and the experiment of Warschauer & Leene [43] which was performed at $Re_D = 1.26 \times 10^6$. The original C_p data in [43] exhibit some spanwise variations; for the purpose of comparison the average value is plotted. Relative to the measurements of Flachsbart (see [45]) at $Re_D = 6.7 \times 10^5$, the LES C_p shows smaller values in the base region. Note that Flachsbart's data contain a kink near $\theta = 110°$, indicating the presence of a separation bubble. This type of separation bubble is characteristic of the critical regime, and is difficult to reproduce experimentally or numerically due to sensitivity to disturbances.

In Table 2.1, we compare the mean drag coefficient, the base pressure coefficient, and the Strouhal number from the LES at $Re_D = 10^6$ with the experimental values. The agreement with the measurements of Shih et al. [38] is reasonably good. The LES somewhat overpredicts the drag coefficient compared with Shih et al. [38], but underpredicts it relative to Achenbach [2] (cf. Figure 2.3). The Strouhal number of 0.22 from Shih et al. is for a rough-surface cylinder; no coherent vortex shedding was observed for smooth cylinders at Re_D larger than 4×10^5. Indeed, it is generally accepted that periodic vortex shedding does not exist in the super-critical regime of flow over a smooth cylinder [45]. From our simulation, a broad spectral peak of the unsteady lift centered at $St \approx 0.28$ is found. It can be argued that although the LES is performed for a smooth cylinder, the discretization of the cylinder surface and the numerical errors due to under-resolution may act as equivalent surface roughness, causing the flow field to acquire some rough-cylinder characteristics. The flow at high Reynolds number is very sensitive to surface roughness and to the level of free-stream turbulence,

6

Table 2.1: Drag, base pressure coefficient and Strouhal number for the flow around a circular cylinder at a Reynolds number of 10^6.

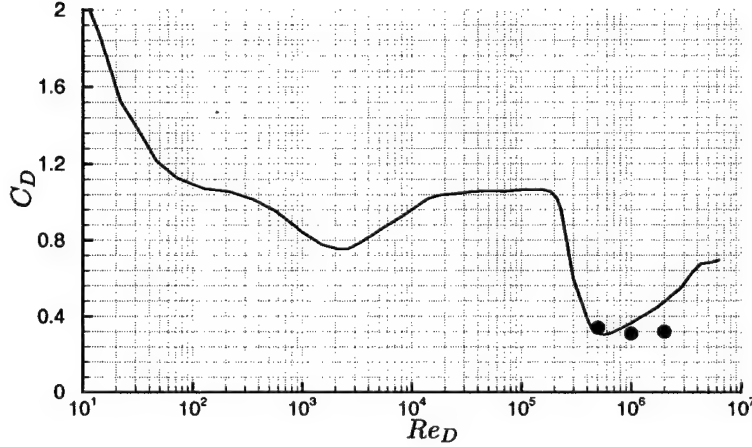|	C_D	$-C_{p,base}$	St
LES	0.31	0.32	0.28
Exp. (Shih *et al.* [38])	0.24	0.33	0.22
Exp. (Others, see [45])	0.17-0.40	–	0.18-0.50

Figure 2.3: Drag coefficient as a function of Reynolds number. ——— , Achenbach [2]; • , Present LES.

which contribute to the wide scatter of C_D and St among various experiments in the literature [45], listed at the bottom of Table 2.1. Other factors causing the data scatter include wind-tunnel blockage and end-plate effects. Our simulation results fall easily within the experimental range. Generally speaking, there is a lack of detailed experimental data at super-critical Reynolds numbers. In particular, velocity and Reynolds-stress profile measurements are non-existent, making a more detailed comparison impossible.

To assess the robustness of the computational method, we have performed simulations at $Re_D = 5 \times 10^5$ and 2×10^6, in addition to the initial attempt at $Re_D = 1 \times 10^6$. The predicted mean drag coefficients are plotted in Figure 2.3 along with the drag curve of Achenbach [2]. While the simulations predict C_D rather well at the two lower Reynolds numbers, the discrepancy becomes large at $Re_D = 2 \times 10^6$. More significantly, the LES solutions show relative insensitivity to the Reynolds number, in contrast to the experimental data which exhibit an increase in C_D with Reynolds number after the drag crisis. Similar Reynolds-number insensitivity has been observed for the other quantities shown previously.

Finally, the skin-friction coefficients predicted by the wall model in the LES calculations are plotted in Figure 2.4 against the experimental data of Achenbach [2] at $Re_D = 3.6 \times 10^6$. The levels are very different on the front half of the cylinder, but are in reasonable agreement on the back half. The boundary-layer separation and the recirculation region are captured rather well by the LES, indicating that they are not strongly affected by the upstream errors. The different Reynolds numbers in the LES and the experiment can account for only a small fraction of the discrepancy. Note that our computed C_f values are comparable to those reported by Travin *et al.* [39] using DES.
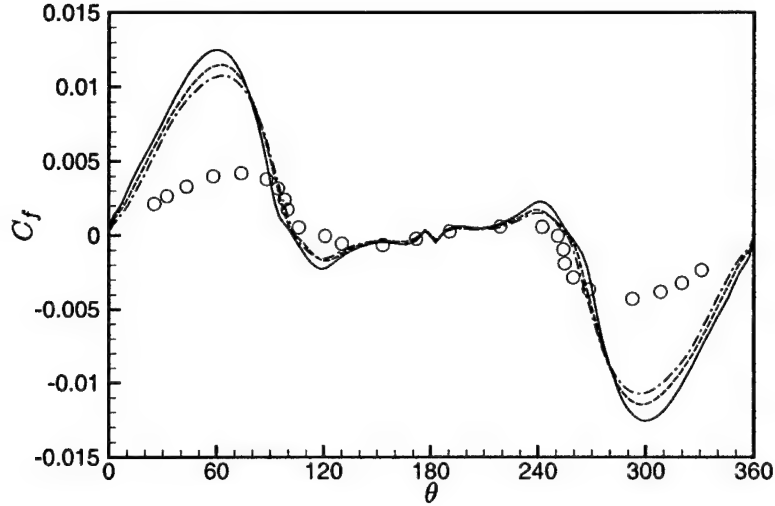
7

Figure 2.4: Skin friction distribution on the cylinder from LES: ———— , $Re_D = 5 \times 10^5$; - - - - , $Re_D = 1 \times 10^6$; —·— , $Re_D = 2 \times 10^6$. ○ , Experiment of Achenbach [2] at $Re_D = 3.6 \times 10^6$.

Travin *et al.* attribute the overprediction of C_f before separation to the largely-laminar boundary layer in the experiment, which has not been modeled adequately in either simulation. Poor grid resolution, which becomes increasingly severe as the Reynolds number increases, is another potential culprit in the present work. In addition, an overprediction of the skin friction by the present wall model has also been observed by Wang & Moin [42] in the acceleration region of the trailing-edge flow, suggesting that this simplified model may have difficulty with strong favorable pressure gradients.

2.3   Concluding remarks

A numerical experiment has been carried out to compute the flow around a circular cylinder at supercritical Reynolds numbers using LES. The simulation is made possible by the use of a simple wall-layer model, Eq. (2.2). The computational solutions correctly capture the delayed boundary-layer separation and reduced drag coefficients consistent with measurements after the drag crisis. In quantitative terms, the mean pressure distributions and overall drag coefficients are predicted reasonably well at $Re_D = 5 \times 10^5$ and 10^6. However, the results are inaccurate at higher Reynolds numbers, and the Reynolds-number dependence of the drag coefficient is not captured. It must be pointed out that the grid used near the cylinder surface, particularly before separation, is quite coarse judged by the need to resolve the outer boundary-layer scales. This is in contrast to the trailing-edge flow case [42] for which the model works well. At such marginal resolution, the SGS modeling errors and numerical errors tend to dominate the LES in the near-wall region, which cannot be corrected by a physical based wall model such as the one employed here. A control-based model, to be discussed in the next chapter, can account for these errors and hence may provide a better alternative. In addition, based on the experimental observation, the boundary layer is largely laminar prior to separation, which has not been modeled adequately by the current wall-layer model.

8

Chapter 3

Wall Modeling Using Optimal Control Techniques

This chapter describes some recent applications of control theory to the wall modeling problem. As noted in Chapter 1, there is evidence that even the analytically correct wall stresses would form a poor LES wall model. Chapter 2 shows that a wall model based purely on physics does not produce accurate solutions for high Reynolds number flows under coarse grid resolution. Hence, it is desirable to formulate a wall model with the capability to compensate for the additional numerical and SGS modeling errors. Since there is no known method for quantitatively determining the exact errors *a priori* (or creating a high fidelity model for them from *a posteriori* data), techniques from optimal control theory have been used to drive the LES system towards a desired state. These techniques were chosen since they seek to minimize a cost function whose minimization should improve the LES results. In doing so, wall stresses that both compensate for the missing physics and the numerical errors can be found.

Optimal control is a branch of control theory that deals with determining the set of controls from some control space of $\mathcal{L}_2$ functions that minimize a given cost function, often denoted as $\mathcal{J}$. There has been and continues to be considerable application of this technique to problems in fluid mechanics. Early applications in conjunction with turbulence simulations involved minimizing drag in a channel [15, 9]. For a review of some of the more recent applications of this approach, see [10] and the references therein. These successes provided evidence that the optimal control technique could be successfully applied in situations with complex physics. A new challenge in the context of wall modeling is to use it in a situation where both the physics and numerics need to be accounted for.

This approach was motivated by two results. The first was the previously mentioned work of Cabot [12] demonstrating that resolved LES wall stresses did not perform well as a wall model. A second result was that of Bagwell *et al.* [7, 6] in their use of linear stochastic estimation (LSE) to derive a wall model. A linear convolution of form $\tau_{i2}^w = L_{ij} * u_j(\cdot, y, \cdot)$ with $i = 1, 3$ and $j = 1, 2, 3$ was used as the wall model. The convolution coefficients, L_{ij} were found using the LSE technique of minimizing the mean square error of this model with DNS training data at $\mathrm{Re}_\tau = 180$ [22]. This model worked well in a channel flow at the same Reynolds number. A channel flow LES was then performed using convolution kernels that were extrapolated to $\mathrm{Re}_\tau = 640$ [6]. In this case, the LSE model performed only marginally better than the shifted model of Piomelli *et al.* [36] (cf. Eq. (1.1)). This result again demonstrates the possibility that the effect of the unmodeled components (numerical and SGS modeling errors) play a significant role in the wall modeling problem. It also shows that if LSE is to be used to develop wall models, the training data must

9

come from an LES at comparable Reynolds numbers. However, these Reynolds numbers are, in general, too high to perform an LES without a wall model. Therefore, a scheme based on optimal control techniques will be used to perform such an LES, thereby generating training data that is at the correct Reynolds number and will account for numerical and SGS modeling errors. The methodology and results are discussed in the remainder of this chapter. They are also described in [32, 33, 5].

3.1 Numerical method

A second-order accurate finite difference scheme is used to discretize the LES equations on a staggered grid system [19]. Given the simple geometry of a channel flow considered in this study, more accurate (spectral) methods could have been used. However, these highly accurate methods are not flexible enough to handle industrial applications with complex geometries (e.g. flow around an airfoil), where both low-order numerics for simplicity and wall modeling for high-Reynolds number boundary layers are needed. A staggered grid system is used to avoid the decoupled pressure-velocity mode as well as the prescription of a boundary condition for the pressure. The time integration is a third-order Runge-Kutta scheme for all the convection and diffusive terms. The diffusive terms in the normal direction to the wall are not treated implicitly since only coarse grid computations are considered. Periodic conditions are imposed in the two directions x_1 and x_3 (or x and z) parallel to the walls so that the Poisson equation can be solved efficiently using a FFT-based Poisson solver.

The subgrid scale model is the Smagorinsky model with the coefficient determined by the plane-averaged dynamic procedure [25]. Unless otherwise stated, all quantities are nondimensionalized by the friction velocity, u_τ, and channel half-height, h. The channel walls are at $y = \pm 1$. The skin friction Reynolds number is then defined as $Re_\tau = u_\tau h/\nu$. When the mean flow is converged in the statistical sense, the mean streamwise pressure gradient is equal to the mean wall stress, that is, $-\partial\langle p\rangle/\partial x = \langle\tau_w\rangle = 1$.

Since 'non-resolved' LES is considered in this study, the classical no-slip boundary condition for the velocity components is replaced by a set of approximate boundary conditions. More precisely, the transpiration velocity (in some cases set to zero) and the two shear stresses τ_{12}^w and τ_{32}^w are provided to the momentum equation in the x_1- and x_3-direction respectively. The sketch in Figure 3.1 shows the location of the variables and boundary conditions in the staggered grid system. The wall normal direction is x_2 (or y) while u_i (or u,v,w) and p are the velocity components and the pressure. The shear stresses τ_{12}^w and τ_{32}^w are prescribed either from one of the wall stress models discussed in Chapter 1 or the optimal control strategy. The wall transpiration velocity is set to zero or determined using the control strategy.

3.2 Optimal formulation

In the process of deriving a new wall model for LES, it is crucial to keep in mind that:

1. The objective is to provide an approximate boundary treatment able to handle very large Reynolds numbers. In this respect, using DNS data as a guide may not be the most judicious choice since these data are only available for low to moderate Reynolds numbers.

2. In any coarse grid LES where the first grid point is within the logarithmic region, the turbulent integral length scale ($L \equiv \kappa y$) is less than half the grid spacing ($\Delta y = y$). As a consequence both sub-grid modeling and numerical errors are important. Therefore the approximate
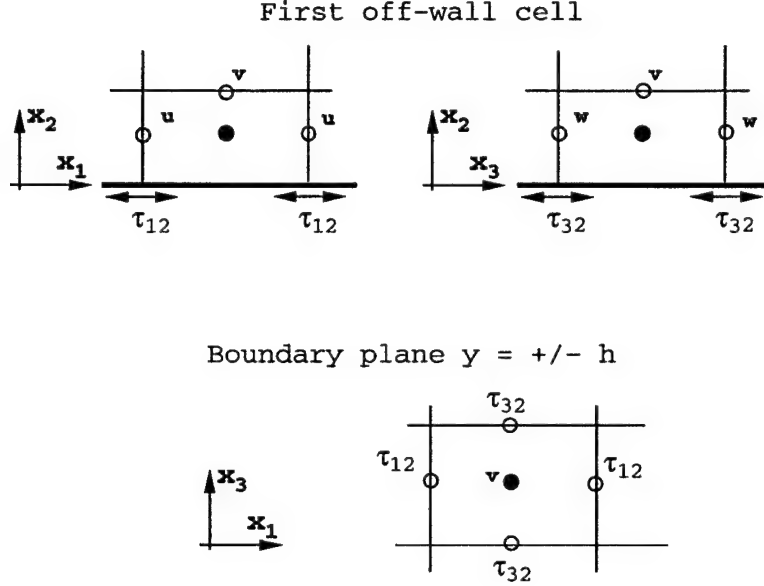
Figure 3.1: Staggered grid system used in this study.

boundary condition should compensate for these errors if the correct mean profile is to be obtained in a coarse grid computation. In this case the best shear stresses to supply are not the physical ones, as from a DNS.

It follows that the reference data used to compare or derive new wall models should be obtained from a high Reynolds number LES simulation on a coarse grid. Of course, such a simulation requires a good model for the near-wall region in the first place. The optimal control framework is applied here to conduct such a simulation without *a priori* knowledge of the necessary wall stress boundary conditions. The case of a channel flow with constant pressure gradient is considered ($\partial \langle p \rangle / \partial x = 1$). The objective is to optimize the shear stresses τ_{12}^w and τ_{32}^w, and in some cases the transpiration velocity v_w, in order to minimize a given cost function. The mathematical formulation is detailed in the following subsections. It is given for the most general case, in which wall stresses and transpiration velocity act as controls, and penalty terms for the deviation from the mean velocity profile, deviation from the rms velocity fluctuations, and control penalty are included in the cost function. Simpler cases may easily be derived by setting certain terms to zero.

3.2.1 State equation

The problem considered is governed by the unsteady, incompressible, filtered Navier-Stokes equations as well as the divergence-free constraint which arises from continuity. The governing equations read:

$$\frac{\partial u_i}{\partial t} + \frac{\partial u_i u_j}{\partial x_j} = -\frac{\partial p}{\partial x_i} + \delta_{i1} + \frac{\partial}{\partial x_j}\left((\nu + \nu_t)\left(\frac{\partial u_i}{\partial x_j} + \frac{\partial u_j}{\partial x_i}\right)\right)$$

$$\frac{\partial u_j}{\partial x_j} = 0,$$

(3.1)

11

where the δ_{i1} represents the constant streamwise pressure gradient. Note that no specific notation is used to describe the spatial filtering associated with the LES formulation. Each variable in the previous and subsequent equations should be understood as a low-pass filtered version of the actual variable (e.g. $u_i \equiv \overline{u_i}$, where the overbar stands for the filtering operator). Eq. (3.1) is valid for any subgrid model based on the Boussinesq assumption. The boundary conditions, specified in terms of the control parameter ϕ defined below, on Eq. (3.1) are:

$$\begin{aligned}
\frac{\partial u}{\partial y_n} + \frac{\partial v_n}{\partial x} &= \frac{1}{\nu_w}\phi_u \\
v_n &= \phi_v \\
\frac{\partial w}{\partial y_n} + \frac{\partial v_n}{\partial z} &= \frac{1}{\nu_w}\phi_w
\end{aligned} \tag{3.2}$$

where the subscript n stands for the outward normal to the wall and ν_w is the wall value of the total dynamic viscosity $\nu + \nu_t$ (in this work $\nu_w \equiv \nu$). The control parameter ϕ is defined as $\phi = (\phi_u, \phi_v, \phi_w) = (\tau_{12}^w, v_w, \tau_{32}^w)$ at $y = +1$ and $\phi = (\phi_u, \phi_v, \phi_w) = -(\tau_{12}^w, v_w, \tau_{32}^w)$ at $y = -1$.

In the classical optimal control procedure the objective is to reduce the given cost function for some period of time. This method has been proven to be efficient [1]. However, this is a very expensive procedure in terms of storage and manipulation of many 3D fields over the entire period under consideration [15]. We therefore make use of a more affordable sub-optimal procedure in which the state equation is first discretized in time, then a control procedure is used to minimize the cost function over a short period of time (the time step) at each time step [9]. This method does not necessarily provide the 'best' answer but it is much more cost effective than the optimal strategy. The equation of state (3.1) is therefore discretized in time by assuming an implicit discretization:

$$u_i^{n+1} + 2\beta\Delta t\left[\frac{\partial P}{\partial x_i} + \frac{\partial u_i u_j}{\partial x_j} - \frac{\partial}{\partial x_j}\left((\nu + \nu_t)\left(\frac{\partial u_i}{\partial x_j} + \frac{\partial u_j}{\partial x_i}\right)\right)\right]^{n+1} = RHS^n$$

$$-2\beta\Delta t\frac{\partial u_j^{n+1}}{\partial x_j} = 0 \tag{3.3}$$

The boundary conditions, Eq. (3.2), apply to Eq. (3.3) and the second order Crank-Nicolson method is recovered if the parameter β is chosen to be $\beta = \frac{1}{4}$. Note that in Eq. (3.3) only the terms involving the solution at the current time step $n + 1$ are written explicitly. This is because in the sub-optimal framework developed in Bewley et al [9], only the terms at time $n + 1$ in the semi-discretized state equation are used in the optimization process. The terms which depend only on the variables at the previous time step n are gathered in the generic notation RHS^n and disappear in the analytical development. Note that there is a slight inconsistency between the time integration used to solve the state equation (explicit third-order Runge-Kutta, Section 3.1) and time integration supposed in the process of defining the control problem (implicit Crank-Nicolson). The optimal control problem and the resulting optimization algorithm proposed in Section 3.2.4 may therefore be considered as only approximation of the 'exact' control problem that should be defined and solved for the flow problem considered. However, in view of the results shown in Sections 3.3 and 3.5, and the small time steps used for the explicit scheme, this approximation is sufficient to provide valuable insight for identifying a practical wall model for coarse grid LES.

3.2.2 Objective function

In the sub-optimal control approach, the boundary conditions (specified by the control parameter ϕ) are used as control to minimize an objective function at each time step. The goal is to provide

numerical boundary conditions to the flow solver so that the overall solution is consistent with what is expected in a channel flow. The objective function is specified as follows:

$$\mathcal{J}(u;\phi) = \sum_{i=1,3} \mathcal{J}_{\text{mean},i}(u;\phi) + \sum_{i=1}^{3} \mathcal{J}_{\text{rms},i}(u;\phi) + \sum_{i=1}^{3} \mathcal{J}_{\text{penalty},i}(\phi). \qquad (3.4)$$

The objective function consists of the three components. $\mathcal{J}_{\text{mean}}$ measures the distance from the plane-averaged LES solution to a desired reference velocity profile. The second component, $\mathcal{J}_{\text{rms}}$ measures the distance from the plane-averaged velocity fluctuation intensities to desired target profiles. Finally, the third component, $\mathcal{J}_{\text{penalty}}$ penalizes the use of large controls ϕ. The component objective functions are defined below.

For the mean streamwise velocity the target or reference profile is taken as a logarithmic velocity profile throughout the channel: $u_{1,\text{ref}}^{+} = \kappa^{-1} \ln y^{+} + C$. The spanwise velocity reference profile is simply $u_{3,\text{ref}} \equiv 0$. The difference between the reference velocity profile and the plane-averaged LES solution is a function of the wall-normal coordinate, y, and can be expressed as

$$\delta_{u_i}(y) = \frac{1}{A} \int \int (u_i - u_{i,\text{ref}}) \, dx \, dz \qquad (i = 1,3) \qquad (3.5)$$

where A is the channel area in the homogeneous plane. Note that any reference profile suitable for a parallel flow could have been used. Notably, a more realistic shape could have been used near the channel center. However, the logarithmic profile is well suited for the near-wall region since we are using a coarse mesh and the Reynolds number, $\text{Re}_\tau = 4000$, is sufficiently high so that the first grid point lies in the logarithmic region ($y^{+} \approx 121$). The mean component of the objective function is then:

$$\mathcal{J}_{\text{mean},i}(u;\phi) = \alpha_i \int_{-1}^{+1} \delta_{u_i}(y)^2 \, dy, \qquad (i = 1,3) \qquad (3.6)$$

Note that there is no need to specify a target profile for the plane-averaged wall-normal velocity since that will be identically zero at each time step provided there is no net transpiration velocity through the boundaries.

The velocity fluctuation intensities are targeted through the $\mathcal{J}_{\text{rms}}$ component of the objective function. The plane-averaged, mean square velocity fluctuations are compared at each time step to the mean square velocity fluctuations, $(u'_{i,\text{ref}})^2$, from the LES of Kravchenko et al. [24] which was performed at the same Reynolds number using a zonally defined mesh to resolve the near-wall region. The distance between the plane-averaged mean square velocity fluctuations and their reference profiles can be measured as

$$\delta_{u'_i}(y) = \frac{1}{A} \int \int \left((u_i - \langle u_i \rangle)^2 - u'^2_{i,\text{ref}} \right) dx \, dz, \qquad (i = 1,2,3), \qquad (3.7)$$

where $\langle u_i \rangle$ denotes the average over the homogeneous directions of the velocity component u_i. The velocity fluctuation intensity component of the objective function is then

$$\mathcal{J}_{\text{rms},i}(u;\phi) = \beta_i \int_{-1}^{+1} \delta_{u'_i}(y)^2 \, dy \qquad (i = 1,2,3) \qquad (3.8)$$

Finally, to prevent numerical instabilities it is necessary to regularize the control, that is, the approximate boundary conditions, by including a penalty component in the overall objective function:

$$\mathcal{J}_{\text{penalty},i}(\phi) = \frac{\gamma_i}{A} \int_{y=\pm 1} \phi_{u_i}^2 \, dx \, dz + \frac{\lambda}{A} \int_{y=\pm 1} \delta_{i2} \phi_{u_2}^4 \, dx \, dz \qquad (i = 1,2,3). \qquad (3.9)$$

13

The first term in the penalty component attempts to prevent the mean square norm of the control parameter from becoming too large. In the case of transpiration velocity control, it was found necessary to prevent the transpiration velocity from becoming too large at any single point, hence the second term in the penalty component (3.9) was added.

Note that each component of the objective function includes a scalar parameter: α_i, β_i, γ_i, or λ. These scalars allow the relative importance of the various objectives to be changed in the overall objective.

3.2.3   Adjoint problem

The gradient of the objective function $\mathcal{J}$ with respect to the control parameter ϕ is estimated by using the Fréchet differential [40] defined for any functional F as:

$$\frac{DF}{D\phi}\tilde{\phi} = \lim_{\epsilon \to 0} \frac{F(\phi + \epsilon\tilde{\phi}) - F(\tilde{\phi})}{\epsilon}, \tag{3.10}$$

where $\tilde{\phi}$ is an arbitrary direction. From Eq. (3.4) the gradient $\mathcal{J}$ is:

$$
\begin{aligned}
\frac{D\mathcal{J}}{D\phi}\tilde{\phi} =\ & \sum_{i=1,3} \alpha_i \int \int \int_{\Omega} 2\frac{\delta_{u_i}}{A}\mathcal{U}_i \, dx \, dy \, dz \\
& + \sum_{i=1}^{3} \beta_i \int \int \int_{\Omega} 2\frac{\delta_{u_i'}(u_i - \langle u_i \rangle)}{A}\mathcal{U}_i \, dx \, dy \, dz \\
& + \lambda\frac{4}{A}\int \int_{y=\pm 1} \phi_{u_2}^3 \tilde{\phi}_{u_2} \, dx \, dz + \sum_{i=1}^{3} \gamma_i\frac{2}{A}\int \int_{y=\pm 1} \phi_{u_i}\tilde{\phi}_{u_i} \, dx \, dz
\end{aligned}
\tag{3.11}
$$

where $\mathcal{U}_i$ denotes the Fréchet derivative of u_i[1]. The gradient of $\mathcal{J}$ cannot be calculated directly from Eq. (3.11) since the derivatives $\mathcal{U}_i$ are unknown.

We now formulate an adjoint problem to find the gradient (3.11). The first step is to take the derivative of Eq. (3.3) with respect to the control ϕ:

$$
\begin{aligned}
\mathcal{U}_i + \Delta t\left[\frac{\partial \mathcal{P}}{\partial x_i} + \mathcal{U}_j\frac{\partial u_i}{\partial x_j} + u_j\frac{\partial \mathcal{U}_i}{\partial x_j} - \frac{\partial}{\partial x_j}\left((\nu + \nu_t)\left(\frac{\partial \mathcal{U}_i}{\partial x_j} + \frac{\partial \mathcal{U}_j}{\partial x_i}\right)\right)\right] &= 0 \\
-\Delta t\frac{\partial \mathcal{U}_j}{\partial x_j} &= 0
\end{aligned}
\tag{3.12}
$$

with boundary conditions:

$$
\begin{aligned}
\frac{\partial \mathcal{U}}{\partial y_n} + \frac{\partial \mathcal{V}_n}{\partial x} &= \frac{1}{\nu_w}\tilde{\phi}_u \\
\mathcal{V}_n &= \tilde{\phi}_v \\
\frac{\partial \mathcal{W}}{\partial y_n} + \frac{\partial \mathcal{V}_n}{\partial z} &= \frac{1}{\nu_w}\tilde{\phi}_w.
\end{aligned}
\tag{3.13}
$$

The right-hand side term in Eq. (3.12) is now zero since the flow field at time step n does not depend on the control ϕ for the current time step. Therefore, the superscript '$n + 1$' has been

---

[1]Technically, the second term in Eq. (3.11) should include the integral $\int \int \int_{\Omega} 2\frac{\delta_{u_i'}(u_i - \langle u_i \rangle)}{A}(\mathcal{U}_i - \langle \mathcal{U}_i \rangle) \, dx \, dy \, dz$, but we make the approximation that $\langle \mathcal{U}_i \rangle \equiv 0$ since $|\langle \mathcal{U}_i \rangle| \ll |\mathcal{U}_i|$ in general.

14

dropped for clarity. Note also in Eq. (3.12) that the Fréchet derivative of the eddy viscosity was assumed to be zero, that is, $D\nu_t/D\phi = 0$. The latter approximation can be justified for short time intervals [14]. Moreover, this system of equations is linear in the variables $\mathcal{U}_i$ and $\mathcal{P}$, where $\mathcal{P}$ is the Fréchet derivative of the pressure. Therefore it can be written in the form:

$$\mathcal{A}\Theta = 0, \tag{3.14}$$

where $\mathcal{A}$ is the linear operator acting on the vector $\Theta = (\mathcal{U}_i, \mathcal{P})^T$. The linear system (3.14) with unknown boundary conditions (3.13) cannot be solved directly; instead, an adjoint operator, $\mathcal{A}^*$, is formulated by considering the equation

$$\langle \mathcal{A}\Theta, \Psi \rangle = \langle \Theta, \mathcal{A}^*\Psi \rangle + \text{BT}, \tag{3.15}$$

where $\langle \cdot, \cdot \rangle$ stands for the inner product defined as the integral over the flow domain of the dot product of the two vectors and Ψ is the adjoint state vector $\Psi = (\eta_i, \pi)^T$. Finding the adjoint operator, $\mathcal{A}^*$, and the boundary terms, BT, is a straightforward exercise in integrating by parts. The adjoint operator acting on the adjoint state vector, that is, $\mathcal{A}^*\Psi$ is defined by the equations:

$$\mathcal{A}^*\Psi = \begin{cases} \eta_i + \Delta t \left[\frac{\partial \pi}{\partial x_i} + \eta_j \frac{\partial u_j}{\partial x_i} - u_j \frac{\partial \eta_i}{\partial x_j} - \frac{\partial}{\partial x_j} \left((\nu + \nu_t) \left(\frac{\partial \eta_i}{\partial x_j} + \frac{\partial \eta_j}{\partial x_i} \right) \right) \right] \\ -\Delta t \frac{\partial \eta_j}{\partial x_j} \end{cases} \tag{3.16}$$

and the boundary terms are:

$$\text{BT} = \Delta t \int \int_{y=\pm 1} (\text{Press} + \text{Conv} + \text{Visc}) \, dx \, dz \tag{3.17}$$

with

$$\begin{aligned} \text{Press} &= \mathcal{P}\eta_{2n} - \mathcal{V}_n\pi \\ \text{Conv} &= \eta_i \mathcal{U}_i v_n \\ \text{Visc} &= -\nu_w \left[\eta_i \left(\frac{\partial \mathcal{U}_i}{\partial y_n} + \frac{\partial \mathcal{V}_n}{\partial x_i} \right) - \mathcal{U}_i \left(\frac{\partial \eta_i}{\partial y_n} + \frac{\partial \eta_{2n}}{\partial x_i} \right) \right]. \end{aligned} \tag{3.18}$$

From Eq. (3.14), the relation (3.15) defining the adjoint operator reduces to

$$\langle \mathcal{A}^*\Psi, \Theta \rangle = -\text{BT}. \tag{3.19}$$

3.2.4 Gradient estimate

We now have the liberty to choose boundary conditions and right-hand side terms for the adjoint problem such that the relation (3.19) can be utilized to calculate the gradient of $\mathcal{J}$. By comparing Eqs. (3.11), (3.17), (3.18) and (3.19), it appears that a judicious choice for the definition of the adjoint problem is:

$$\mathcal{A}^*\Psi = \frac{2}{A} \begin{pmatrix} \alpha_1 \delta_u + \beta_1 \delta_{u'}(u - \langle u \rangle) \\ \beta_2 \delta_{v'}(v - \langle v \rangle) \\ \alpha_3 \delta_w + \beta_3 \delta_{w'}(w - \langle w \rangle) \\ 0 \end{pmatrix} \tag{3.20}$$

with boundary conditions at the wall:

$$\begin{aligned} \eta_1 v_n + \nu_w \frac{\partial \eta_1}{\partial y_n} &= 0 \\ \eta_{2n} &= 0 \\ \eta_3 v_n + \nu_w \frac{\partial \eta_3}{\partial y_n} &= 0. \end{aligned} \tag{3.21}$$

15

In doing so, Eq. (3.19) can be re-written as:

$$\frac{D\mathcal{J}}{D\phi}\tilde{\phi} = -\Delta t \int\int_{y=\pm 1}\left[\eta_1\tilde{\phi}_u + \left(\pi - 2\nu_w\frac{\partial\eta_{2n}}{\partial y_n}\right)\tilde{\phi}_v + \eta_3\tilde{\phi}_w\right]dx\,dz$$

$$+\lambda\frac{4}{A}\int\int_{y=\pm 1}\phi_{u_2}^3\tilde{\phi}_{u_2}\,dx\,dz + \sum_{i=1}^{3}\gamma_i\frac{2}{A}\int\int_{y=\pm 1}\phi_{u_i}\tilde{\phi}_{u_i}\,dx\,dz$$

Since Eq. (3.22) is valid for all directions $\tilde{\phi}$, the gradient of $\mathcal{J}$ may be extracted:

$$\begin{aligned}
\frac{D\mathcal{J}}{D\phi_1} &= \Delta t\eta_{1,w} + \frac{2\gamma_1}{A}\phi_1 \\
\frac{D\mathcal{J}}{D\phi_2} &= \Delta t\left(\pi_w - 2\nu_w\frac{\partial\eta_{2n}}{\partial y_n}\right) + \frac{2\gamma_2}{A}\phi_2 + \frac{4\lambda}{A}\phi_2^3 \\
\frac{D\mathcal{J}}{D\phi_3} &= \Delta t\eta_{3,w} + \frac{2\gamma_3}{A}\phi_3,
\end{aligned} \qquad (3.22)$$

where the subscript w stands for the values at the wall. A control procedure using a simple steepest descent algorithm at each time step may now be proposed such that:

$$\phi^{n+1,k+1} = \phi^{n+1,k} - \mu\frac{D\mathcal{J}(\phi^{n+1,k})}{D\phi} \qquad (3.23)$$

where the parameter μ can be varied to change the rate of convergence and the extra superscript k refers to the subiterations in the descent algorithm. Note that the adjoint operator depends on the state vector $(u_i, P)^T$ at time $n+1$ so that the state equation and the adjoint problem must be solved simultaneously to obtain the sub-optimal approximate boundary conditions. The following algorithm is used a each time step of the flow solver to obtain the optimized boundary conditions:

1. Start with the state vector $(u_i, P)^T$ at time n, the adjoint vector $(\eta_i, \pi)^T$ and control parameter ϕ at sub-iteration n_k,

2. Use Eq. (3.20) with boundary condition (3.21) to compute the adjoint vector at sub-iteration n_{k+1}. For this purpose, the operator for the adjoint velocity, Eq. (3.16), is re-written as:

$$\frac{1}{2}\eta_i^{n_{k+1}} + \frac{1}{2}\eta_i + 2\beta\Delta t\left[\frac{\partial\pi}{\partial x_i} + \eta_j\frac{\partial u_j}{\partial x_i} - u_j\frac{\partial\eta_i}{\partial x_j} - \frac{\partial}{\partial x_j}\left((\nu + \nu_i)\left(\frac{\partial\eta_i}{\partial x_j} + \frac{\partial\eta_j}{\partial x_i}\right)\right)\right] \qquad (3.24)$$

where only the first term is taken at sub-iteration n_{k+1}, the others being considered at sub-iteration n_k. A Poisson equation is solved for the adjoint pressure at each sub-iteration to enforce the divergence-free condition on $\eta_i^{n_{k+1}}$.

3. Compute the gradient of the cost function at sub-iteration n_{k+1} by using Eq. (3.22),

4. Compute the control parameter ϕ at sub-iteration n_{k+1} by using Eq. (3.23),

5. Compute the $\mathcal{L}_2$-norm of the difference $\phi^{n_{k+1}} - \phi^{n_k}$.

6. If it is more than 0.1% of the $\mathcal{L}_2$-norm of ϕ^{n_k}, then go back to step 1. Otherwise, use ϕ_u and ϕ_w as approximate boundary conditions to compute the state vector at time $n+1$.

16

3.2.5   Validating the gradient of the objective function

To validate the gradient computation, finite difference approximations to the gradient were calculated. This is relatively simple to do. Given a control vector ϕ and a velocity field u, choose a small value of ϵ and perturb the control vector at one point by the amount ϵ (e.g. add ϵ to τ_{12}^w at one point on the lower wall) to obtain a new control vector $\phi + \epsilon\tilde{\phi}$. Now advance the velocity field one time step and explicitly calculate the value of the objective function (3.4), that is, calculate $\mathcal{J}(\phi + \epsilon\tilde{\phi})$. The approximate gradient in the direction $\tilde{\phi}$ is then:

$$\frac{D\mathcal{J}}{D\phi}\tilde{\phi} \approx \frac{\mathcal{J}(\phi + \epsilon\tilde{\phi}) - \mathcal{J}(\phi)}{\epsilon} \tag{3.25}$$

By comparing the approximation (3.25) to a centered difference approximation, it was found that $\epsilon = 10^{-3}$ produces good approximations to the gradient. By successively perturbing the control vector ϕ at every point, it is possible to approximate the entire gradient $D\mathcal{J}/D\phi$. This finite difference gradient approximation can then be compared to the gradient approximated by the adjoint problem described above.

It was found that the correlation between the two gradient approximations was generally in excess of 80%. When the transpiration velocity was not included in the control, the correlation was generally in excess of 90%. Thus we are led to believe that the adjoint problem defined above may be yielding satisfactory approximations to the gradient of the objective function, but further work is necessary to determine if the gradient approximation can be improved.

3.3   Results: optimal control without transpiration velocity

Several LES's have been performed to test the optimal control strategy described in the previous section. We first investigate the case when only the wall stress boundary conditions are used as control. The wall normal velocity is set to zero at the boundary: $v_n = \phi_v = 0$. In addition, we consider an objective function for mean flow only, by setting β_i to zero. The α_i's are taken such that $\alpha_1 = \alpha_3 = 1$. Several numerical tests were performed to fix the coefficients μ, γ_1, and γ_3. It was found that the value $\mu = 5 \times 10^3$ ensured good convergence of the steepest descent algorithm, while $\gamma_1 = \gamma_3 = 4 \times 10^{-5}$ ensured that the whole algorithm is stable.

3.3.1   Statistics

In this section, the grid is uniform in all directions with $32 \times 33 \times 32$ cells and the domain size is $(2\pi h, 2h, 2\pi h/3)$ where h is the channel half height. The Reynolds number based on the friction velocity u_τ and h is 4000. In wall units, the grid spacing is $\Delta x^+ \approx 785$, $\Delta y^+ \approx 242$ and $\Delta z^+ \approx 262$. Since a staggered mesh system is used, the first u velocity point is located at $y^+ \approx 121$. At this coarse resolution, most of near-wall turbulent structures cannot be captured so that an effective wall model is necessary to compensate. The computation was run for a sufficiently long period to be statistically independent of the initial condition and then statistics were accumulated over a time period of order $20\, h/u_\tau$.

Figure 3.2 shows the mean velocity profile from the LES in which the optimal procedure of Section 3.2 was used to obtain the approximate boundary condition. The mean value of τ_{12}^w was either provided by the optimal procedure itself or re-computed so that the first point coincides with the logarithmic law $\langle u \rangle^+ = 2.41 \ln y^+ + 5.2$. The results are very similar in the two cases. The overall agreement is much better than with the shifted model [36], Eq. (1.1), which is also shown in Figure 3.2 for easier comparison. An artificial boundary layer still develops between the second
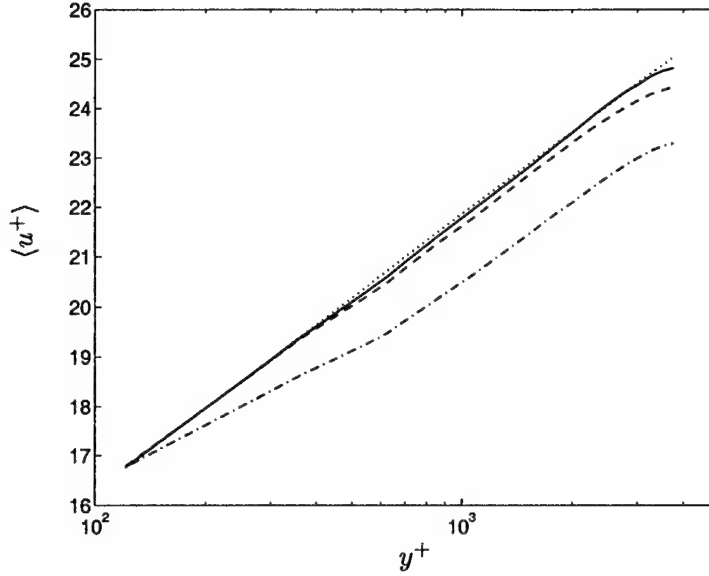
17

Figure 3.2: Mean velocity profiles for $\mathrm{Re}_\tau = 4000$. ——— , control includes wall stresses and transpiration; - - - - , control includes wall stresses only; — $\cdot$ — , no control, uses wall stress model of [36]; $\cdots\cdots$, logarithmic reference profile, $u^+_{\mathrm{ref}} = 2.41 \ln y^+ + 5.2$.

and the third grid point but its amplitude is much smaller than with the shifted model. The deficit in the log-law intercept is of order 0.25 compared to 1.35 in [36].

Note that the optimized wall stress boundary conditions produce a mean velocity profile that is nearly exact for the first two grid points. The small error in the channel interior is believed to be due to the sub-optimal formulation in which the wall stresses are optimized only over each time step. However, the result in Figure 3.2 shows a clear improvement in comparison with the shifted model. An additional computation was performed where only τ^w_{12} was optimized (u_3 was set to zero at the wall), resulting in a mean velocity profile is intermediate between the two previous computations. The conclusion is that both τ^w_{12} and τ^w_{32} must be optimized (or modeled carefully) if a velocity profile close to the target one is sought. The case of control with wall stresses and transpiration velocity is also plotted in Figure 3.2, which will be discussed later in Section 3.4.

3.3.2 Shear stress structure

From Eq. (1.1), the wall shear stresses in the LES with the shifted model should be perfectly correlated with the velocity components at the first plane, shifted in the upstream direction by the amount Δ_s. This is shown in Figure 3.3 which displays typical iso-lines of τ^w_{12}, u, τ^w_{32} and w. The upstream shift is only a fraction of the cell size, viz. $\Delta_s \approx 0.67\Delta x$, and is hardly visible in the figure. Both τ^w_{12} and u are characterized by elongated structures in the streamwise direction while τ^w_{32} and w are characterized by more rounded structures in the $x-z$ plane. The reference data from the sub-optimal computation are plotted in Figure 3.4. The perfect correlation between the wall stresses and the velocity components at the first off-wall plane no longer holds. The streamwise velocity u still displays elongated structures in x as well as τ^w_{32}. In contrast, τ^w_{12} and w are less elongated. Eight fields from the sub-optimal LES have been used to compute correlation coefficients between the velocity gradients, the velocity components at the first off-wall plane and the wall stresses.
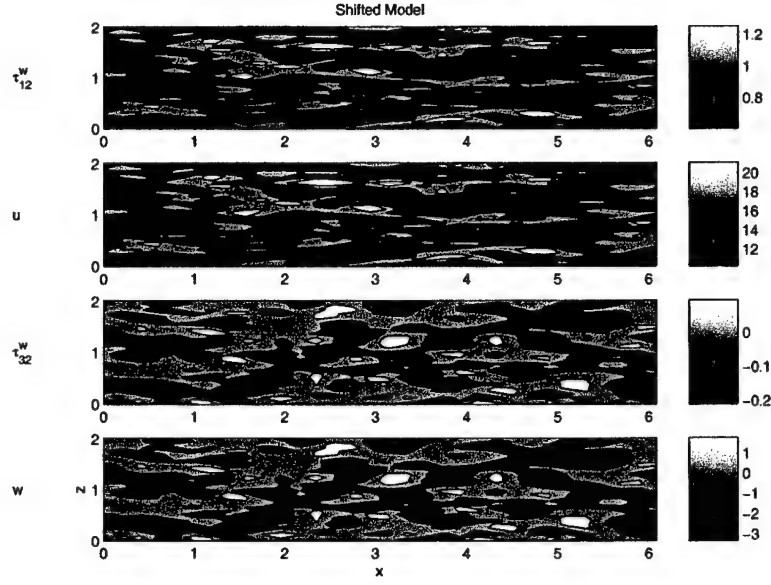
18

Figure 3.3: From top to bottom: Contours of τ_{12}^w, u, τ_{32}^w and w from the LES with the shifted model of Piomelli *et al.* [36] at $\mathrm{Re}_\tau = 4000$. The velocity components are from the first off-wall plane.

The best results (those with the correlation greater than 0.3) are reported in Figure 3.5. The position of the perfect correlations between τ_{12}^w and u, τ_{32}^w and w which are assumed in the shifted model [36], Eq. (1.1), is also reported. Note that in the sub-optimal calculation, τ_{12}^w is almost not correlated with the streamwise velocity downstream shifted by Δ_s. The correlation is better when an upstream shifted version of u is used instead. On the other hand the maximum of correlation between τ_{32}^w and w is located close to the assumed downstream shift Δ_s. The best correlation for τ_{12}^w is found with the spanwise derivative of w, whereas τ_{32}^w best correlates with du/dz. Other non negligible correlation coefficients are found between τ_{12}^w and du/dx, and τ_{32}^w and dv/dz. No clear picture is available yet to explain these correlations. Finally, note the fairly good and somewhat expected negative correlation between τ_{12}^w and v. This correlation supports the underlying idea in the ejection model of Piomelli *et al.* [36]. A more systematic way of exploiting correlations between the approximate boundary condition and the velocity field close to the wall is presented in Section 3.5.

3.3.3 Discussion

The reduced deficit in the intercept with the sub-optimal computation is associated with a better representation of the gradient of the mean velocity profile within the first few grid points. This is better seen in Figure 3.6 which displays the quantity $\kappa y^+ \, d \langle u \rangle^+ / dy^+$ as a function of the distance to the wall. Theoretically, this quantity should be equal to unity in the case where the sub-optimal strategy is used since the value of κ is taken to be $\kappa = 1/2.41$, consistently with the target velocity profile $\langle u \rangle^+ = 2.41 \ln y^+ + 5.2$. For the case where the shifted model [36], Eq. (1.1), is used, this quantity is not expected to be exactly unity since the value picked for κ is somewhat arbitrary. However this quantity is constant if the mean profile follows a logarithmic behavior. Practically, $\kappa y^+ \, d \langle u \rangle^+ / dy^+$ is not found to be equal to unity when computed from the exact log profile $\langle u \rangle^+ = 2.41 \ln y^+ + 5.2$ because of the large errors associated with the second-order finite
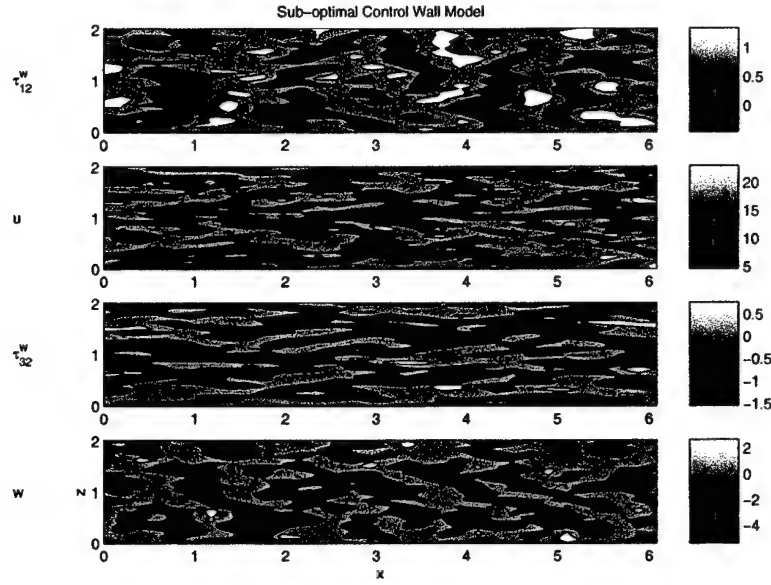
19

Figure 3.4: From top to bottom: Contours of τ_{12}^w, u, τ_{32}^w and w from the LES with the sub-optimal strategy at $\text{Re}_\tau = 4000$. The velocity components are from the first off-wall plane.
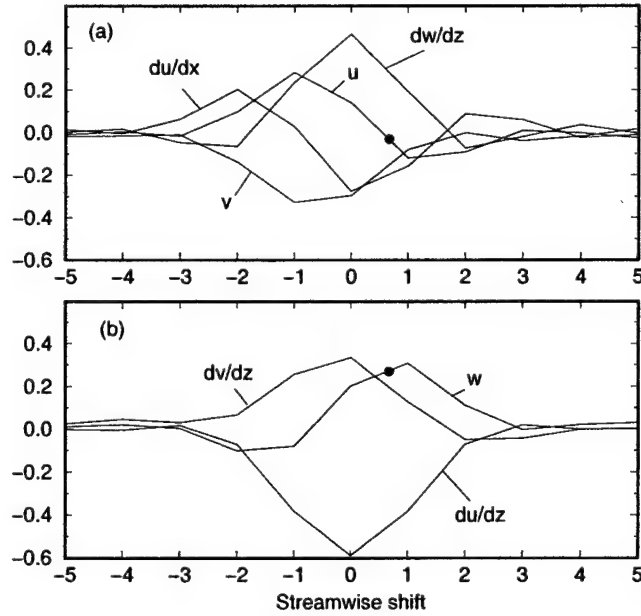

Figure 3.5: Best correlation coefficients for (a) τ_{12}^w, (b) τ_{32}^w. ——— , sub-optimal computation; $\bullet$, shows the position where the correlation between τ_{12}^w and u, and τ_{32}^w and w in the shifted model of Piomelli *et al.* [36] is assumed to be unity.

20
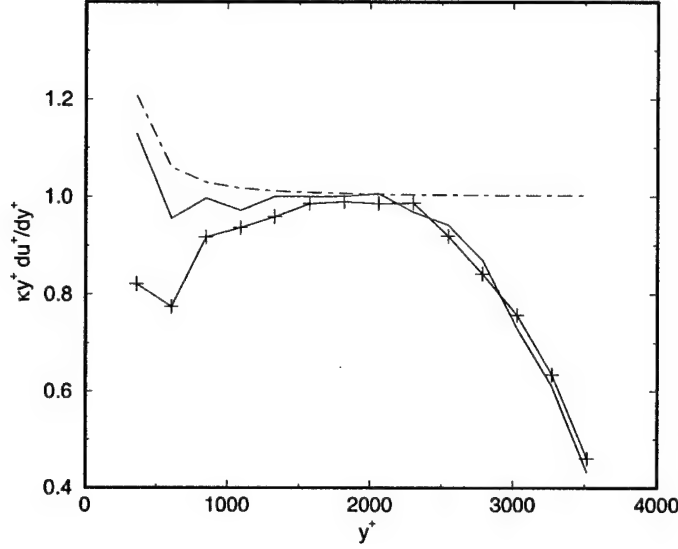
Figure 3.6: Non-dimensionalized mean velocity gradient $\kappa y^+ \, d\langle u \rangle^+ / dy^+$ for $\mathrm{Re}_\tau = 4000$. ——— , sub-optimal computation; —+— , Shifted model of Piomelli *et al.* [36]; - - - - , not exact differentiation applied to $\langle u \rangle^+ = 2.41 \ln y^+ + 5.2$.

differences on the coarse grid considered. This is shown in Figure 3.6 which also demonstrates that the non-dimensionalized mean gradient from the sub-optimal computation follows closely (to within 8%) its value from the exact log law. The mean gradient from the computation with the shifted model [36] is 25% below its expected value, which explains the deficit in the intercept observed in Figure 3.2.

The mean velocity gradient appears in the mean momentum equation which reads:

$$\langle u'v' \rangle = y + \nu \frac{\partial \langle u \rangle}{\partial y} + \left\langle \nu_t \frac{\partial u}{\partial y} \right\rangle \tag{3.26}$$

This equation reduces to:

$$\frac{\partial \langle u \rangle}{\partial y} \approx \frac{\langle u'v' \rangle - y}{\nu + \langle \nu_t \rangle} \tag{3.27}$$

under the usually well verified assumption $\left\langle \nu_t \frac{\partial u}{\partial y} \right\rangle \approx \langle \nu_t \rangle \left\langle \frac{\partial u}{\partial y} \right\rangle$. Eq. (3.27) reveals that for a given amount of eddy viscosity, the mean velocity gradient is directly related to the difference between the total $(-y)$ and resolved $(-\langle u'v' \rangle)$ shear stress, viz. $\langle u'v' \rangle - y$, the larger the difference the larger the gradient. This is confirmed in Figure 3.7 which shows that the artificial condition provided by the sub-optimal strategy leads to an equilibrium in which the resolved part of the stress is smaller. It is also worth noting that the quantity $\langle u'v' \rangle - y$ is quite different in the two computations but that the absolute value of the resolved stress are both close to unity $(|\langle u'v' \rangle|_{\max} \approx 0.9$ for the computation with the shifted model of Piomelli *et al.* [36], $|\langle u'v' \rangle|_{\max} \approx 0.86$ for the sub-optimal case). Since there is a large difference in the velocity gradient (it is 30% higher in the sub-optimal case), the production of kinetic energy $-\langle u'v' \rangle \, d\langle u \rangle / dy$ is necessarily greater in the
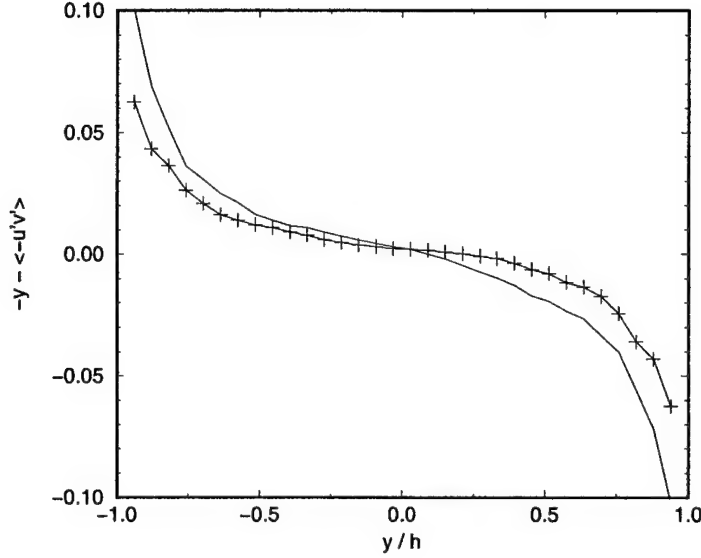
21

Figure 3.7: Difference between the total and the resolved stress for $Re_\tau = 4000$. —— , sub-optimal computation; —+— , Shifted model of Piomelli *et al.* [36].

sub-optimal case, as shown in Figure 3.8a. Figure 3.8b shows that this is also true for the dissipation rate of kinetic energy, a direct consequence of the fact that production and dissipation balance reasonably well in this high-Reynolds number channel flow. Note that the total dissipation is very well approximated by the subgrid scale (SGS) dissipation $\epsilon_{sgs} = \langle 2\nu_t S_{ij} S_{ij} \rangle$ that has been reported in Figure 3.8b. The SGS dissipation can further be approximated (to within a few percents) by $\epsilon_{approx} = 2 \langle \nu_t \rangle \langle S_{ij} S_{ij} \rangle$. The form of the approximate dissipation ϵ_{approx} indicates that the sub-optimized boundary condition can act on the flow field and generate an equilibrium with higher dissipation in the near wall region by either increasing the mean eddy-viscosity or increasing the velocity fluctuations. The mean eddy-viscosity profiles in the two computations are found to be almost identical (not shown). The turbulent fluctuations are higher in the sub-optimal case than in the shifted model [36] computation, see Figure 3.9. The agreement with the fully-resolved LES data of Kravchenko *et al.* [24] turns out to be better with the sub-optimized boundary condition regarding the normal and spanwise direction, worse regarding the streamwise direction. In any case, the reasoning given above indicates that the increase in the turbulent fluctuations when the sub-optimal strategy is used, Figure 3.9, is consistent with the previous findings on the mean velocity gradient, Figure 3.2, resolved shear stress, Figure 3.7, turbulence production and dissipation, Figure 3.8.

Similar results have been obtained for two other Reynolds numbers, namely $Re_\tau = 640$ and 20000 (not shown). For the first case, the mean velocity profile from the sub-optimal computation is slightly closer to the logarithmic law than that obtained from the shifted model [36]. For the case $Re_\tau = 20000$, the deficit in the intercept is the same than for the case $Re_\tau = 4000$, viz. 0.25. Also the profiles of turbulent fluctuations do not change if plotted in outer coordinates y/h. This means that the asymptotic regime in terms of Reynolds number has been reached: results of the same quality as above can be obtained for arbitrarily large Reynolds numbers with the same coarse
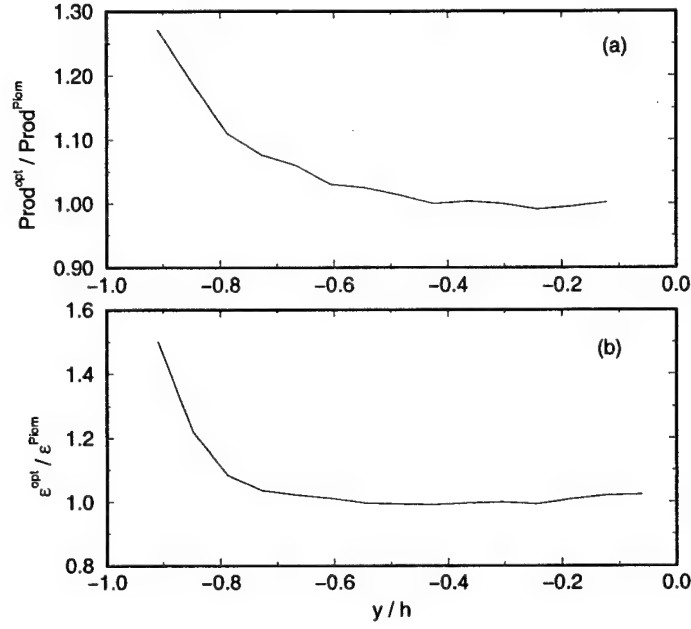
22

Figure 3.8: Turbulence (a) production (b) subgrid scale dissipation from the sub-optimal computation scaled by the same quantity from the LES with the shifted model of Piomelli *et al.* [36] for $Re_\tau = 4000$.
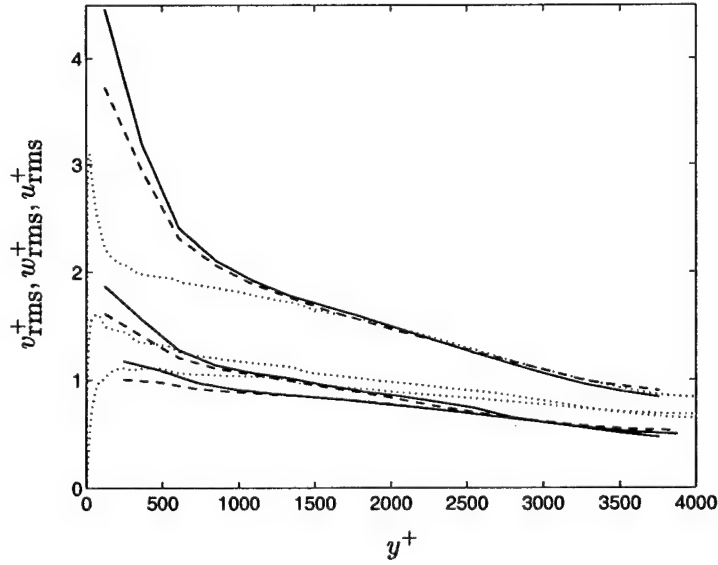

Figure 3.9: Root-mean-square of velocity fluctuations with objective to control mean flow only. ——— , control includes wall stresses and transpiration; ---- , control includes wall stresses only; ········ , reference profiles from [24].

23

grid.

3.4 Results: optimal control with transpiration velocity

The results presented in the previous section were computed assuming that the wall-normal velocity is identically zero at the boundary. However, since the no-slip boundary condition cannot be applied without adequate near-wall resolution, perhaps it does not make sense to insist that the velocity normal to the boundary is zero. After all, a wall model should capture the effects of the near-wall turbulence on the outer flow, including such hallmarks of near-wall turbulence as ejections and sweeps. The combination of non-zero boundary-normal velocity with wall stresses should allow the wall model to influence more of the computational domain than wall stress boundary conditions alone, since the boundary-normal velocity affects the entire flow directly via the continuity equation.

3.4.1 Objective function for mean flow only

Transpiration velocity is now added to the control set to determine if there is an improvement of the prediction of the mean velocity profile. To test the influence of transpiration velocity only on the mean velocity profile, the constants β_i in the objective function, Eq. (3.4), are set to zero so that only the desired mean velocity profile is targeted. For this simulation the parameters in the objective function (3.4) were: $\alpha_1 = \alpha_3 = 1, \beta_1 = \beta_2 = \beta_3 = 0, \gamma_1 = \gamma_3 = 10^{-4}, \gamma_2 = 0.02$, and $\lambda = 0$. The relaxation parameter in the steepest descent algorithm was $\mu = 10^3$.

The new mean velocity profile is plotted in Figure 3.2 as the solid line, which shows that, indeed, the addition of the transpiration control improves the mean profile slightly over the case when only wall stress controls are considered. Also shown in Figure 3.2 is the mean velocity profile obtained by using the simple wall stress model of [36], Eq. (1.1), that correlates the streamwise wall stress to the streamwise velocity at a point away from the wall and slightly downstream. The latter model yields results that are typical of most current wall stress models for this flow configuration.

The improvement in the mean velocity profile is encouraging. However, this is obtained at the expense of turbulence intensity. Figure 3.9 shows the root mean square (rms) velocity fluctuations for the sub-optimal wall stress boundary conditions with and without the addition of transpiration velocity control. The rms velocity fluctuations actually increase with the addition of transpiration, which is certainly in the wrong direction since the fluctuation intensities are already over-predicted.

3.4.2 Objective function including mean flow and rms velocities

In this case, the objectives of matching the rms velocities of Kravchenko et $al.$ [24] are added into the cost function. For this simulation the parameters in the objective function (3.4) were: $\alpha_1 = \alpha_3 = 1, \beta_1 = \beta_2 = \beta_3 = 3 \times 10^{-4}, \gamma_1 = 5 \times 10^{-5}, \gamma_2 = 10^{-3}, \gamma_3 = 4 \times 10^{-6}$ and $\lambda = 5 \times 10^{-3}$. The relaxation parameter in the steepest descent algorithm was $\mu = 500$ for ϕ_{u_2} and 10^5 for ϕ_{u_1} and ϕ_{u_3}.

Figure 3.10 shows the rms velocities when the rms component is included in the objective function. As illustrated in Figure 3.10, the prediction of the rms velocities improves when the transpiration velocity control is added; however, the streamwise rms velocity is still over-predicted near the wall. Not shown for this simulation is the mean velocity profile, which in this case is not as good as the mean velocity profile that is achieved in the previous section when only the mean velocity profile is targeted by the controls. If shown, it would lie between the two mean velocity profiles in Figure 3.2 corresponding to control by wall stress only and control by wall stress plus
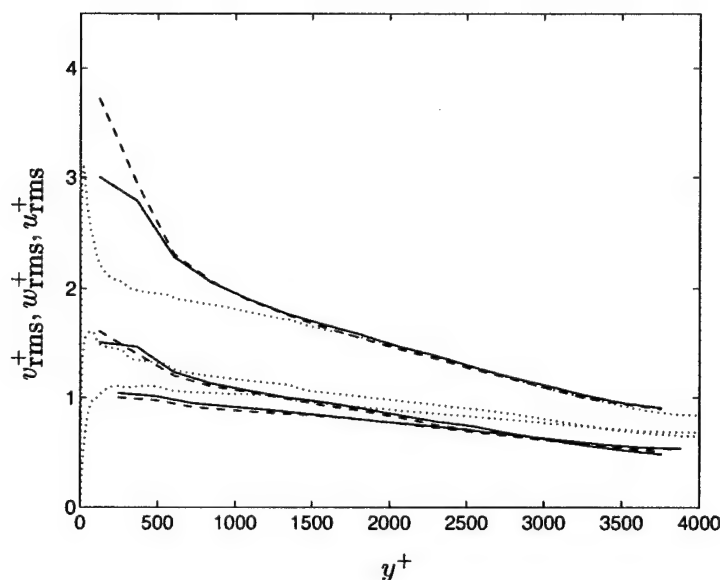
Figure 3.10: Root-mean-square of velocity fluctuations with objective to control mean flow and rms velocities. ——— , control includes wall stresses and transpiration; - - - - , control includes wall stresses only; ········ , reference profiles from [24].

transpiration velocity. Furthermore, the region in which the improved predictions occur is limited to approximately the first three grid cells adjacent to the wall.

The results of this simulation show that the prediction of velocity fluctuation intensities can be improved by the addition of a wall-normal velocity approximate boundary condition. But, the fact that the mean velocity profile is not as well predicted when the velocity fluctuations are targeted through the objective function suggests that the objectives of getting the correct mean velocity profile *and* the correct rms velocities may be competing objectives.

3.5 A simpler wall model from LSE of wall stress data

While the sub-optimal control strategy for generating wall stresses could be used as a wall model for coarse-grid LES, its cost is approximately 20 times greater than of an LES on the same grid compared to an explicit wall stress model such as Eq. (1.1). Furthermore, a target mean velocity profile must be provided to define the objective function. It may be possible to lower the cost of control strategy, but that possibility is not investigated here. The real strength of the optimal control strategy is that it yields wall stress boundary conditions that work for coarse-grid, high Reynolds number LES. Thus, a reference data set can be generated against which new wall models can be compared. The reference data can even be used to derive new wall models. Such an approach is described in this section.

The most desirable wall stress model would be similar to Eq. (1.1) in that it would be an explicit relation between the wall stresses and the velocity field. One could, for instance, require the wall stress model to be the best possible mean square estimate of the sub-optimal wall stress as a function of the velocity field in a neighborhood of the point where the wall stress is required. This is the conditional average of the wall stress given the local velocity field (a conditional average is

necessary because the wall stress may have a stochastic, or unpredictable, component with respect to the local velocities). It is denoted by $\langle \tau_{i2}^w(x,z)|\mathbf{E} \rangle$, where $\mathbf{E}$ is a vector of events. In the present study, $\mathbf{E}$ will be a vector containing the local velocity field, but it could easily contain pressure, velocity gradients, quadratic products, or any other quantities which might characterize the wall stresses. The conditional average embodies so much statistical information that it is unlikely that it could be found exactly, but it can be approximated by its linear stochastic estimate (LSE), given by (see [3] for instance):

$$\langle \tau_{i2}^w(x,z)|\mathbf{E} \rangle \approx \check{\tau}_{i2}^w(x,z) = L_{ij}E_j \qquad i = 1,3, \quad j = 1,2,3,\dots,N, \qquad (3.28)$$

where N is the number of events being considered, and L_{ij} are estimation coefficients relating τ_{i2}^w to E_j. By the statistical orthogonality principle [34], the mean square error between τ_{i2}^w and $\check{\tau}_{i2}^w$ is minimized when the event data are uncorrelated with the error $e_i = \tau_{i2}^w - \check{\tau}_{i2}^w$:

$$\langle e_i E_k \rangle = \langle (\tau_{i2}^w - \check{\tau}_{i2}^w)E_k \rangle = 0. \qquad (3.29)$$

Substituting Eq. (3.28), the estimation coefficients L_{ij} are governed by:

$$\langle \tau_{i2}^w E_k \rangle = L_{ij}\langle E_j E_k \rangle. \qquad (3.30)$$

The matrix $\langle E_j E_k \rangle$ is invertible provided the events are linearly independent. Thus, to obtain the LSE, the correlations $\langle \tau_{i2}^w E_k \rangle$ and $\langle E_j E_k \rangle$ must be found and the events must be selected that best characterize the wall stress.

Though the technique employed here is essentially the same as that of Bagwell *et al.* [7], the results are different since the reference data used here is already known to work well for a coarse grid LES, whereas Bagwell's reference data comes from a direct numerical simulation at low Reynolds number. As will be shown below, an event field consisting of the nearby velocities is sufficient to yield wall models of the form (3.28) that have greater than 80% correlation with the optimal wall stresses. Moreover, the new wall models, when used in an LES, will be shown to reproduce the results of the sub-optimal control LES.

3.5.1 LSE predictions

To implement the LSE, eight velocity fields, well separated in time, and their sub-optimal wall stresses from the $\mathrm{Re}_\tau = 4000$ simulation discussed in Section 3.3 were used. In implementing the LSE, it was found that better results were obtained by estimating only the fluctuating part of the wall stresses from the fluctuating part of the velocity field. To this end, the instantaneous plane averaged wall stress was subtracted from the wall stresses and the average over the first off-wall plane of the horizontal velocity was subtracted from its velocity component for each sample. The LSE can be written as a convolution sum in the wall-parallel, homogeneous directions. The exact form of the LSE wall model for the fluctuating part of the wall stresses is given by:

$$
\begin{aligned}
\check{\tau}_{12}^{w'}|_{m,n} = \quad & \sum_{k=-n_z}^{n_z}\sum_{j=1}^{n_y}\sum_{i=-n_x}^{n_x} L_{ijk}^{11}\left[u_{m-i,j,n-k} - \langle u(\cdot,y_1,\cdot)\rangle\right] \\
& + \sum_{k=-n_z}^{n_z+1}\sum_{j=1}^{n_y}\sum_{i=-n_x}^{n_x-1} L_{ijk}^{13}w_{m-i,j,n-k}, \qquad (3.31)
\end{aligned}
$$

26

$$\check{\tau}_{32}^{w'}\big|_{m,n} = \sum_{k=-n_z}^{n_z-1}\sum_{j=1}^{n_y}\sum_{i=-n_x}^{n_x+1} L_{ijk}^{31}\left[u_{m-i,j,n-k} - \langle u(\cdot, y_1, \cdot)\rangle\right]$$
$$+ \sum_{k=-n_z}^{n_z}\sum_{j=1}^{n_y}\sum_{i=-n_x}^{n_x} L_{ijk}^{33} w_{m-i,j,n-k}, \tag{3.32}$$

where the parameters n_x, n_y, n_z determine the number of velocity points used in the convolution sums to estimate the wall stress at each wall location (denoted by the subscript pair m, n). Note that the summation relating $\tau_{12}^{w'}$ and the spanwise velocity w has different indices than the summation for u in Eq. (3.31). This is due to the staggered grid. Also note that the wall-normal velocity does not appear in the LSE wall model. This is because the wall-normal velocity is linearly dependent on the wall-parallel velocities and thus cannot be used as an independent event in the LSE. The coefficients L^{11}, L^{13}, L^{31}, and L^{33}, are determined by requiring that the error be orthogonal to the events (velocities) as in Eq. (3.29).

For an *a priori* comparison of the wall stress fluctuations predicted by the LSE and those of the optimal strategy one possibility is to compute the correlation coefficient:

$$C_{i2} = \frac{\langle \check{\tau}_{i2}^{w'} \tau_{i2}^{w'}\rangle}{\langle(\check{\tau}_{i2}^{w'})^2\rangle^{1/2}\langle(\tau_{i2}^{w'})^2\rangle^{1/2}}, \tag{3.33}$$

where $i = 1, 3$ and the average denoted by, $\langle\cdot\rangle$, is taken over all of the samples. Another frequently used quantity for comparison is the relative mean square error:

$$R_{i2} = \frac{\langle(\check{\tau}_{i2}^{w'} - \tau_{i2}^{w'})^2\rangle}{\langle(\tau_{i2}^{w'})^2\rangle}, \tag{3.34}$$

where, again, $i = 1, 3$.

Table 3.1 shows the correlation coefficients and relative mean square error for several choices of the parameters n_x, n_y, and n_z. The first noteworthy observation is that the correlations between the sub-optimal wall stress fluctuations and those predicted by the LSE, Eqs. (3.31) and (3.32) increase significantly when velocity data is included from the first two wall-parallel planes (compare $n_y = 1$ and $n_y = 2$). The estimates with $n_x = 15$ and $n_z = 15$ use nearly all of the velocity data in each wall-parallel plane, but note that this results in little improvement over the comparable $n_x = 4, n_z = 4$ results. Figures 3.11–3.14 show contour plots of the LSE coefficients for the case $n_x = 2, n_y = 2, n_z = 2$. Each figure contains two plots, the top plot corresponding to the first plane of velocity data and the bottom plot to the second. The plots indicate several symmetries in the LSE coefficients. For example L^{11} is symmetric with respect to reflection in the spanwise direction whereas L^{13} is anti-symmetric. These symmetries could be exploited to reduce the number of free coefficients in a wall model, but we have not explored that here.

Bagwell *et al.* [7] used entire planes of velocity data to form the LSE, but as results in Table 3.1 suggest, a small number of data points may be sufficient. These *a priori* results suggest that the LSE can reproduce the sub-optimal wall stress fluctuations reasonably well, but even correlations in excess of 80% do not guarantee that the LSE can perform well as a wall model. This can only be checked via an actual simulation.

3.5.2 LSE wall model results

The LSE was used to model the fluctuating portion of the wall stresses in terms of the velocity field and must be combined with a model for the mean wall stress to be used as an LES wall model.
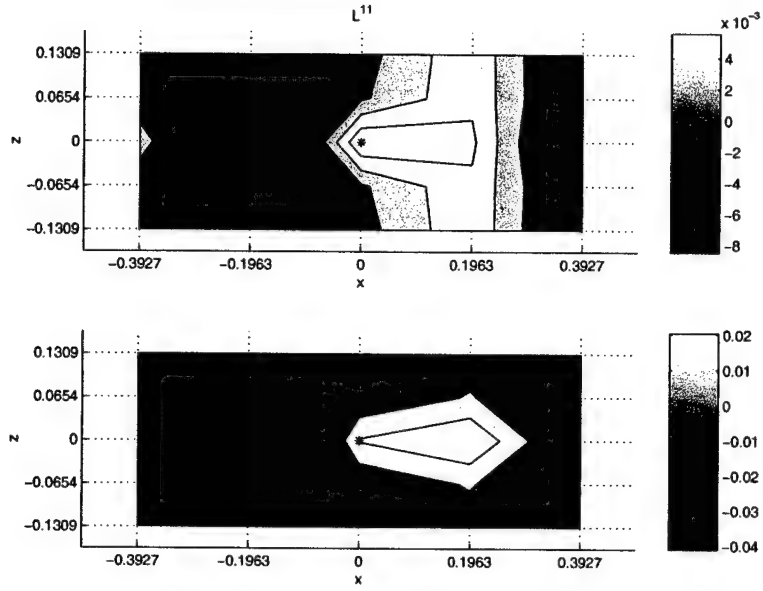
Figure 3.11: Contours of LSE coefficient L^{11} for $n_x = 2, n_y = 2$, and $n_z = 2$, in the xz-plane. The top plot is for the first plane $(j = 1)$ and the bottom plot is for the second plane.
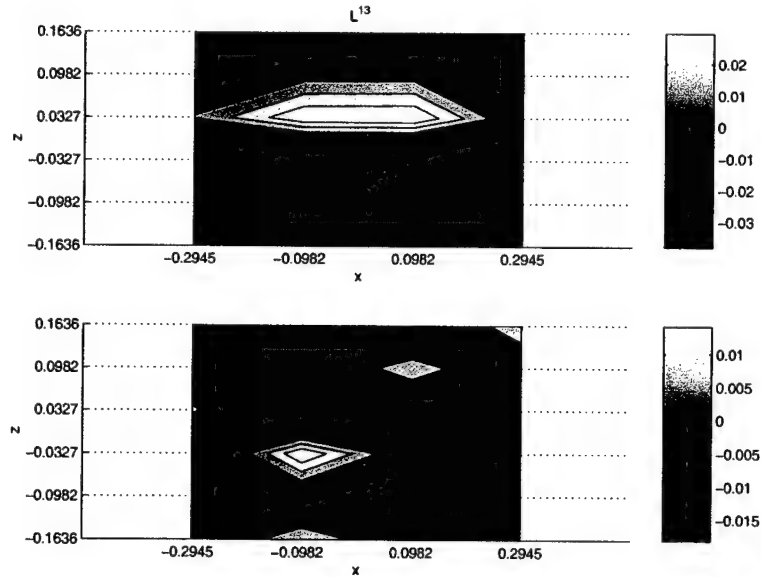

Figure 3.12: Contours of LSE coefficient L^{13}. Refer to Figure 3.11 for details.
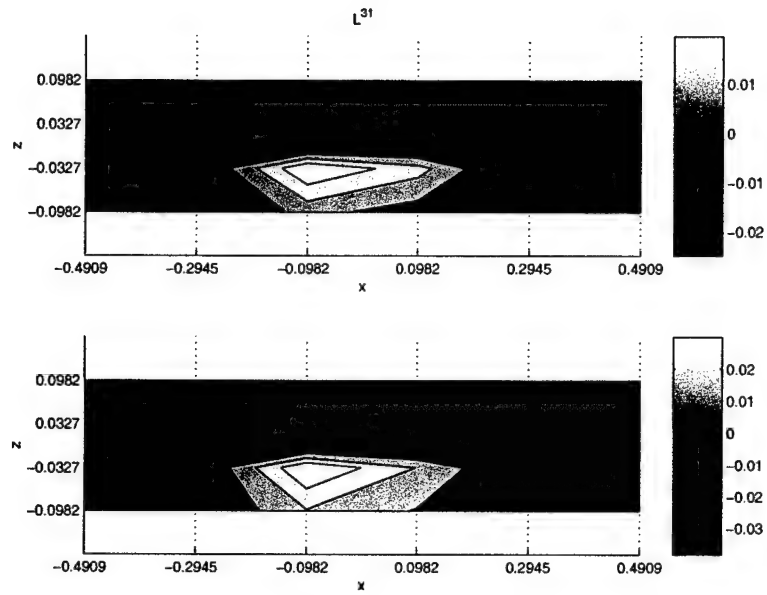
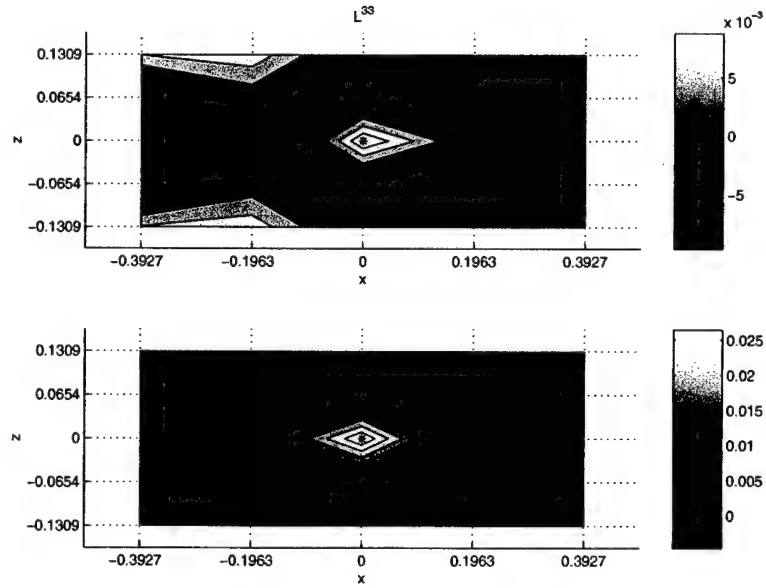Figure 3.13: Contours of LSE coefficient L^{31}. Refer to Figure 3.11 for details.

Figure 3.14: Contours of LSE coefficient L^{33}. Refer to Figure 3.11 for details.

Table 3.1: Correlation coefficients and relative mean square errors for the LSE wall model fluctuations versus the sub-optimal wall stress fluctuations for different numbers of velocity data use in the estimates. The fifth line, set apart by horizontal lines, is for the coefficients used as an actual wall model in Section 3.5.2.

n_x	n_y	n_z	C_{12}	C_{32}	R_{12}	R_{32}
1	1	1	.45	.59	.78	.65
4	1	4	.48	.64	.77	.59
15	1	15	.51	.66	.74	.57
1	2	1	.73	.82	.46	.32
2	2	2	.76	.89	.42	.21
4	2	4	.78	.91	.40	.18
15	2	15	.79	.91	.37	.18
2	3	2	.79	.90	.42	.21
4	3	4	.81	.92	.34	.15

The actual model used is:

$$\tau_{12}^w|_{m,n} = \langle \tau_{12}^w \rangle + \check{\tau}_{12}^{w'}|_{m,n} \tag{3.35}$$

$$\tau_{32}^w|_{m,n} = \check{\tau}_{32}^{w'}|_{m,n}, \tag{3.36}$$

where $\check{\tau}_{12}^{w'}$ and $\check{\tau}_{32}^{w'}$ are given by Eqs. (3.31) and (3.32), respectively. The mean wall stress $\langle \tau_{12}^w \rangle$ is found by assuming that the plane-averaged streamwise velocity at the first off-wall grid location and the mean wall stress are related by the logarithmic law of the wall:

$$\langle u_1(\cdot, y_1, \cdot) \rangle = \langle \tau_{12}^w \rangle^{1/2} \left[2.41 \log(\frac{y \langle \tau_{12}^w \rangle^{1/2}}{\nu}) + 5.2 \right]. \tag{3.37}$$

By using the LSE wall model (3.35) in the same flow discussed in Section 3.2.1, with $Re_\tau = 4000$ and the same resolution, it was found that the wall models based on the one plane LSE, $n_y = 1$ resulted in mean velocity profiles (not shown here) that were not as good as the profiles from the sub-optimal simulation. However, the wall model based on the two plane LSE was able to reproduce nearly exactly the results of the sub-optimal simulation. Shown in Figure 3.15 is the mean velocity profile from a simulation with an LSE wall model of the form (3.35) with $n_x = 2, n_y = 2$, and $n_z = 2$. Simulations with LSE models based on smaller stencils of velocity data did not work as well, whereas LSE models based on larger stencils reproduced the sub-optimal results. The turbulent fluctuations are also in perfect agreement with those of the sub-optimal wall stress simulation; see Figure 3.16.

These results are remarkable in that the wall stress model (3.35) reproduces the results of the sub-optimal simulation at a cost only slightly higher than that of a simulation with no wall model. However, the model given by Eq. (3.35) will not be of much use if new coefficients need to be derived for different Reynolds numbers or for different grid resolutions. Fortunately, we have found that simulations with Eq. (3.35) perform well over a large range of Reynolds numbers using the same coefficients derived from the $Re_\tau = 4000$ sub-optimal data. Figure 3.17 shows the results of using Eq. (3.35) at Reynolds numbers: $Re_\tau = 640, 4000$, and 20000. The simulations were conducted on the same uniform grid as the $Re_\tau = 4000$ simulation with the log law, Eq. (3.37), used to determine the mean wall stress. In the $Re_\tau = 640$ LES, the log law was used to relate the plane-averaged
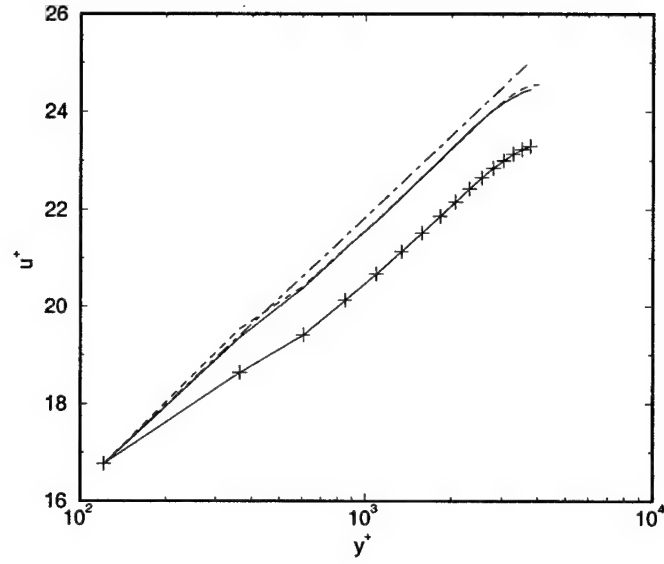
Figure 3.15: Mean velocity profiles for $Re_\tau = 4000$. ——— , sub-optimal computation; ——+— , Shifted model of Piomelli *et al.* [36]; ---- , LSE model; —·— , $\langle u \rangle^+ = 2.41 \ln y^+ + 5.2$.
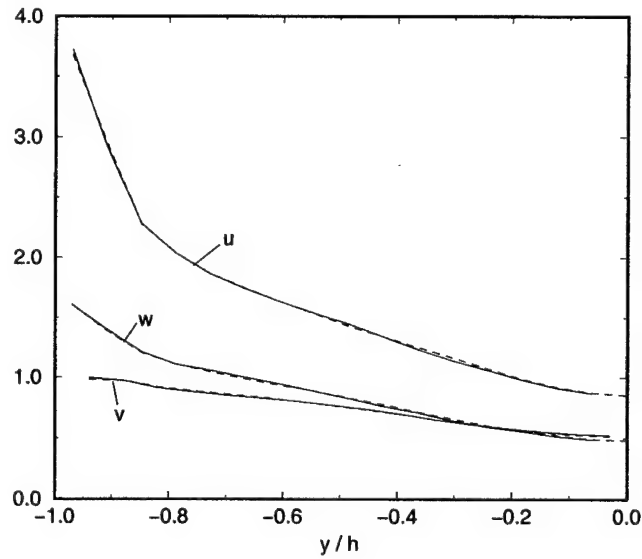

Figure 3.16: Root-mean-square of velocity fluctuations for $Re_\tau = 4000$ and uniform $32 \times 33 \times 32$ grid. ——— , sub-optimal computation; ---- , LSE model.
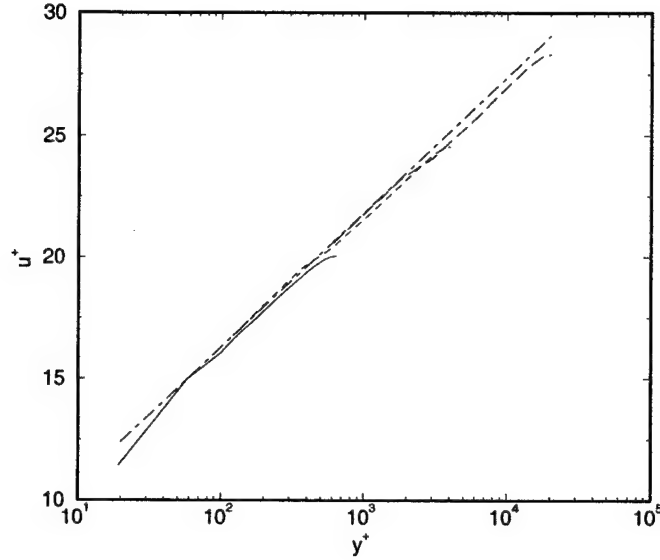
Figure 3.17: Mean velocity profiles from LES's with the LSE model on uniform $32 \times 33 \times 32$ grid: ——— , $Re_\tau = 640$; ---- , $Re_\tau = 4000$; ——— , $Re_\tau = 20000$; —·— , $\langle u \rangle^+ = 2.41 \ln y^+ + 5.2$.

streamwise velocity from the second plane to the mean wall stress because the first plane is in the buffer region at $y^+ \approx 20$.

Similarly, the same coefficients were used with Eq. (3.35) in a simulation with a refined grid at $Re_\tau = 20000$. The number of cells was doubled in each direction to $64 \times 65 \times 64$. The resulting mean flow profile is shown in Figure 3.18. The log region intercept is still slightly underpredicted, but the mean flow now exhibits a wake-like behavior near the channel center as has been observed in high Reynolds number channel simulations in which the near-wall region is resolved [24].

Unfortunately, this simple linear model is not going to be a panacea. Figure 3.19 shows the mean velocity profiles for several channel flow LES's at $Re_\tau = 4000$, all using the same number of grid points as the simulations discussed above and using the simple linear wall stress model previously derived. In each case some reasonable modification has been made. For instance, a fully conservative fourth order finite difference scheme was used, and, as shown in the figure, the mean-velocity is under-predicted. To test the effects of the numerics on the efficacy of the wall model, two different things were tried: stretching the grid in the wall-normal direction and modifying the dynamic procedure as suggested by [13]. As Figure 3.19 shows, the simple linear wall stress model performs worse in every one of these cases than in the original simulation for which it was designed.

3.6 Conclusion

A suboptimal control strategy has been successfully applied to a coarse grid LES of a channel flow at high Reynolds number. The two objectives of this study are: 1) to demonstrate that a control strategy can determine approximate wall boundary conditions that result in an accurate LES, and 2) to find a simple wall model using these results. In both cases, the work can be judged
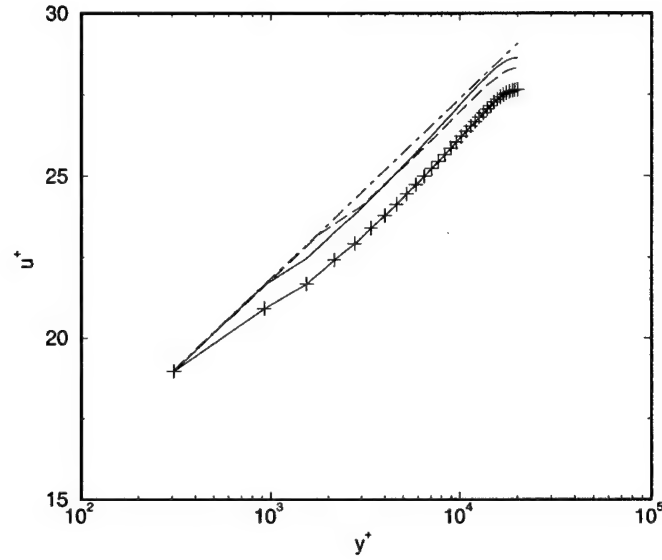
Figure 3.18: Mean velocity profiles from LES's for $Re_\tau = 20000$ and different uniform grids. ——— , $64 \times 65 \times 64$ grid points and LSE model; ——— , $32 \times 33 \times 32$ grid points and LSE model; ——+— , $64 \times 65 \times 64$ grid points and shifted model of Piomelli *et al.* [36]; —·— , $\langle u \rangle^+ = 2.41 \ln y^+ + 5.2$.
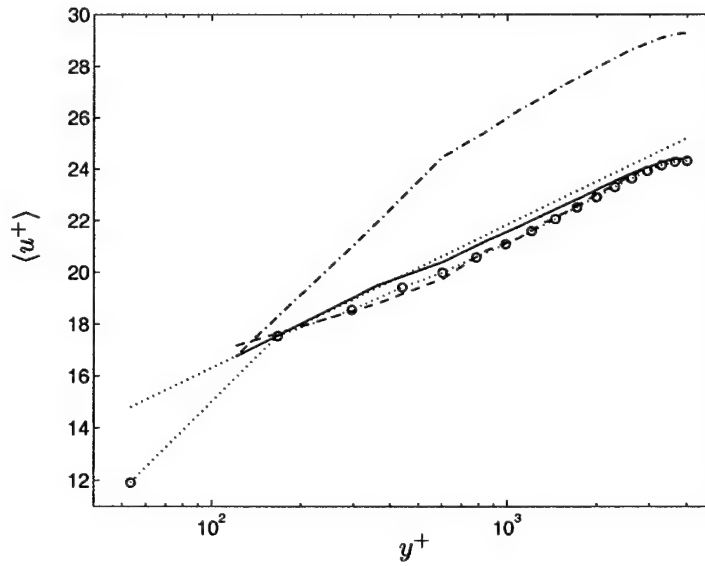

Figure 3.19: Mean velocity profiles using fixed, simple linear model for the wall stresses. ········ , logarithmic reference profile $u^+_{\text{ref}} = 2.41 \ln y^+ + 5.2$; ——— , model reproduces mean profile when used in same setting that it was derived; ---- , same model with fourth-order finite differences; —·— , same model with modified dynamic procedure as in [13]; ·· o ·· , same model with stretched wall-normal grid.

a partial success. The sub-optimally controlled LES, using both wall stresses only and wall stresses and transpiration velocity, is able to generate mean velocity profiles in good agreement with the logarithmic law. It is also determined that the wall stresses provide most of the control authority in this situation. However, the rms velocity fluctuations, particularly the streamwise component near the wall, are not well predicted using this scheme when the objective function includes the mean flow only. When the objective function is enhanced to include a component targeting the reference rms velocity fluctuations of Kravchenko [24], modest improvement is observed, but the streamwise rms velocity remains overpredicted near the wall. Furthermore, the objective of matching the rms velocity fluctuations appears to compete with the objective to match the mean velocity, resulting in a slightly less accurate mean profile.

The data generated from the simulations using wall stress control only have been used to derive a LSE model which predicts the wall stresses from the near-wall velocity field. The LSE model is found to work well over a wide range of Reynolds numbers using the same grid and numerical methods. However, when applied to LES at the same Reynolds number that the training data are generated, but with different numerical methods, the same model is found to perform poorly. This provides additional evidence that non-physical errors, namely numerical and SGS modeling errors, play a critical role in the wall modeling problem and must be addressed for an adequate solution to be found.

Chapter 4

New Directions in Control-Based Wall Modeling

Many important lessons were learned from the control based wall modeling work discussed in the previous chapter. Unfortunately, this approach is impractical due to the high computational cost required for the suboptimal control, which requires both the solution of adjoint equations and many iterations to achieve convergence in the wall stresses. Furthermore, the cost function is based on known target data, making the model non-predictive. The LSE models generated from such computations are too sensitive to the numerical parameters to construct a universal LSE coefficient database. Thus, a low-cost, robust wall model is needed to achieve the accuracy of the sub-optimal control technique without an *a priori* target solution. To this end, a cost function based on a RANS solution will be constructed in Section 4.1 to make the model predictive, and in Section 4.2, the problem will be formulated in an optimal shape design setting in an attempt to reduce the computational cost. Some test results and discussions are presented in Sections 4.3 and 4.4.

4.1   Cost function

In order to make the wall model predictive, an easy-to-evaluate cost function near the wall using quantities not known *a priori* must be defined. To this end, a RANS model is used to provide the target velocity. This is motivated by the recognition that the near-wall region of a high Reynolds number boundary layer is more appropriately modeled by RANS than by a coarse grid LES with filter length larger than the integral scale of the turbulence.

In the present work, the RANS model is obtained from the simplified version of the TBL equation model introduced in Chapter 2,

$$\frac{d}{dy}\left[\left(\nu + \nu_t\left(y\right)\right)\frac{du_i}{dy}\right] = \frac{1}{\rho}\frac{\partial p}{\partial x_i}\bigg|_{\mathrm{LES}}, \quad i = 1, 3 \tag{4.1}$$

$$\nu_t\left(y\right) = \kappa\nu y^+\left(1 - e^{-y^+/A}\right)^2, \quad y^+ = yu_\tau/\nu.$$

These equations model all Reynolds stresses through a damped mixing-length eddy viscosity, and explicitly account for the pressure gradient which is assumed constant across the wall layer and is imposed by the LES. To complete the model, a no slip condition is applied at the wall and the outer boundary is set to be the LES velocity. The resulting velocity profile should be interpreted as the ensemble averaged velocity profile given the local LES state. It can therefore be expected that, on average, the resolved LES should match the RANS solution near the wall. Note that this

model is chosen for simplicity in this initial attempt, and there are likely better models for this application that will be explored in future work.

In an overlapped region consisting of N LES grid points in the wall-normal direction, cost functions are devised to match the LES and RANS solutions on average. An attractive method in a statistically stationary flow would be to use a running time average to provide the target velocities. However, if the control authority is restricted to the current time, this approach becomes impractical since the flow at the current time would contribute only a small fraction of the total cost function. This makes it difficult to determine the control since the cost function is insensitive to it. If the control is explicitly computed as a function of time, then adjoint equations have to be integrated backward in time to find a correct solution over a sufficiently large time window which contains enough statistical samples.

An alternative is to use the current state as the statistical sample. Thus, the first cost function is defined to be the $\mathcal{L}_2$ difference between the LES and RANS states:

$$
J_{\mathcal{L}_2} = \int_S \sum_{n=1}^{N} \left((u_{\mathrm{RANS},1}|_{y_n} - u_{\mathrm{LES},1}|_{y_n})^2 + (u_{\mathrm{RANS},3}|_{y_n} - u_{\mathrm{LES},3}|_{y_n})^2 \right) dS, \tag{4.2}
$$

where S is the surface and y_n are the locations of the n overlap points. In this way, a sufficient number of samples of the flow state are used to make a meaningful average. Also, the cost function is based only on quantities at the current time step, so no history information is required. This type of cost function is also compatible with the gradient evaluation methods used in this work (see Section 4.2).

Other cost functions can also be formulated for this problem. A cost function based on the average deviation of the LES and RANS is:

$$
J_A = \left(\int_S \sum_{n=1}^{N} ((u_{\mathrm{RANS},1}|_{y_n} - u_{\mathrm{LES},1}|_{y_n}) + (u_{\mathrm{RANS},3}|_{y_n} - u_{\mathrm{LES},3}|_{y_n})) \, dS \right)^2. \tag{4.3}
$$

This cost function is similar to that used in [33]. However, as shown in Section 4.3, this cost function performs quite poorly. Analysis of its gradients indicates that they do not capture the sign information correctly in some regions (gradient computation will be discussed in the next section). In order to retain more information and move in the direction of feedback control, a signed cost function has also been used:

$$
J_S = \int_S \sum_{n=1}^{N} ((u_{\mathrm{RANS},1}|_{y_n} - u_{\mathrm{LES},1}|_{y_n}) + (u_{\mathrm{RANS},3}|_{y_n} - u_{\mathrm{LES},3}|_{y_n})) \, dS. \tag{4.4}
$$

When this cost function is used, the control strategy is shifted to force the cost function to zero rather than minimizing it. It was thought that this approach might better take advantage of the method being used for gradient evaluation, but it only resulted in a moderate improvement (see Section 4.3).

The choice of N in Eqs. (4.2)–(4.4) should be made to include as many matching layers as possible while remaining in the region where the RANS model is a reasonable approximation for the given local flow. Furthermore, the LES velocity too close to the wall may involve large errors (see [12]) and thus is not suitable as a RANS boundary condition. In the calculations presented in this article, N has been chosen to be three.

Two important points should now be noted. First, while all the cost functions here are based on matching RANS and LES velocities, other quantities could also be used. These could include

36

matching vorticity or energy fluxes with suitable models. Second, it may not be possible or desirable to reduce the cost function to zero. Doing so could artificially reduce the turbulence fluctuations of the flow. Also, if an inexpensive scheme is required, it may not be possible to fully optimize the solution. Thus, the cost function must act as a suitable quantity for feedback regulation, rather than for minimization.

4.2 Optimization using shape design techniques

Optimal shape design consists of a set of techniques for optimizing a shape to achieve an engineering objective (e.g. [31]). Several approaches have been developed in this field that have had some success in reducing the computational expense of the optimization procedure. In an attempt to bring these techniques to bear, the wall modeling problem is formulated in this framework.

In general, the formulation is to consider a partial differential equation $A(U, q, a) = 0$ in a region Ω satisfying boundary conditions $b(U, q, a) = 0$ on $\partial\Omega$. The optimization is performed to determine

$$\min_{a} \left\{ J(U, q, a) : A(U, q, a) = 0 \; \forall x \in \Omega, b(U, q, a) = 0 \; \forall x \in \partial\Omega \right\} \tag{4.5}$$

for some cost function $J(U, q, a)$. In this formulation, U is the state, q the shape, and a are the control variables. The gradient of the cost function with respect to the control variables is then:

$$\frac{dJ}{da} = \frac{\partial J}{\partial a} + \frac{\partial J}{\partial q}\frac{\partial q}{\partial a} + \frac{\partial J}{\partial U}\frac{\partial U}{\partial q}\frac{\partial q}{\partial a}. \tag{4.6}$$

The standard technique for solving this equation is to use an adjoint method interfaced with a gradient minimization technique. But, as previously noted, this can be expensive and present data storage difficulties in time-accurate computations. Since it is the last term in Eq. (4.6) that requires the adjoint evaluation, Mohammadi & Pironneau [31] suggest the following assumption when the controls and the cost function share the same support:

$$\frac{dJ}{da} \approx \frac{\partial J}{\partial a} + \frac{\partial J}{\partial q}\frac{\partial q}{\partial a}. \tag{4.7}$$

This assumption is called the method of incomplete sensitivities since the sensitivity to the state gradient is ignored. The use of this method has been explored in this work since it has produced positive results in the optimization of aerodynamic shapes. For examples, see [29, 30, 31], although these are all steady, two-dimensional applications. Since no rigorous proof on the applicability of this technique exists and its usefulness is based on purely empirical studies, it was not known how well it would perform in a full LES. Furthermore, the present cost function is not defined exactly on the support of the control, although it is defined in a small neighborhood of the control. While these factors will produce errors, the gradient evaluation needs only accurately predict the sign of the gradient and capture to some degree the difference in magnitudes of the derivatives with respect to different control parameters. A goal of this work is to determine if the amount of information contained in this gradient is sufficient for application to wall boundary conditions.

In order to apply the incomplete sensitivity assumption, the control must be related to shape design parameters. B-splines spaced evenly along the surface (although not enough to form a complete basis) are used to parameterize deformations normal to the surface. The control parameters, a_i, are then the spline amplitudes. The gradient of the cost function with respect to these parameters can be computed using finite differences by perturbing each parameter by a small value, ϵ, and then using Eq. (4.7) to evaluate the gradient based on the current state information. It is not

necessary to recompute the actual geometry or grid because all the state variables of interest can be stored and matched to the new surface. The parameter ϵ is chosen *a priori* by making it small enough such that the gradient values are independent of it.

Once the cost function gradient is known, the new spline amplitudes can be computed by

$$a_i^{k+1} = a_i^k - \rho \frac{\partial J}{\partial a_i}, \tag{4.8}$$

where ρ is a descent parameter set in advance and k is the iteration count. The new shape is computed by adding the surface perturbations to the previous shape. To relate this to the wall stresses, the RANS model is used to compute the correction to the equivalent slip velocity on the original surface:

$$u_{w,i}^c = f_{\text{RANS},i}(y_{new}), \quad i = 1, 3, \tag{4.9}$$

where f stands for the RANS model given by Eq. (4.1). This approach is inspired by a Taylor series expansion about the wall [31]. In this way, it is not necessary to change the computational geometry of the LES.

The total slip velocity is given by adding the correction $u_{w,i}^c$ to the old wall slip velocity. Corrected wall stresses can then be computed directly by definition

$$\tau_{w,i} = \tau_{w,i}^o + \frac{1}{Re} \frac{-u_{w,i}^c}{\Delta x_2}, \tag{4.10}$$

where Δx_2 is the local wall normal grid spacing.

While this approach avoids the evaluation of a set of adjoint equations, iterations are still required to converge the solution. Additional function evaluations are also often used to determine an optimal choice for ρ at each iteration. In order to make the wall model practical, these costs must be avoided. Therefore, no iterations are performed at each time step. The cost function gradients are computed and used in a feedback manner to provide a correction. Every a_i is reset to zero at each time step. Also, ρ is taken to be a fixed parameter similar to the gain in a feedback controller. To make up for some of this lost information, a predictor-corrector approach to the control algorithm will be used. This is done by using Eq. (4.1) to compute a prediction of the wall stress before the optimization is used. It is expected that the prediction will account for the missing physics in the coarse grid LES while the optimization will correct for the numerical and SGS modeling errors. While this approach must be classified as sub-optimal, it is still reasonable to expect a cost function reduction if at each time step the LES velocity is forced in the direction of the reduced cost function.

4.3 Results

The application of this method to the trailing edge flow simulated previously by Wang & Moin [41, 42] has produced mixed results. The first goal is to justify the incomplete sensitivities assumption. The $\mathcal{L}_2$ cost function history is shown in Figure 4.1. While the average value is reduced approximately 15% from the initial value, this is not completely out of the range of the cost function fluctuations. It is therefore inconclusive regarding the validity of the assumption. As shown in Figure 4.2, the predicted wall stress matches the full LES wall stress quite well in some regions for the $\mathcal{L}_2$ and signed cost functions, but performs poorly in other regions. The separation point is predicted reasonably accurately for both these cost functions. As previously indicated, the average cost function performed more poorly. Figure 4.3 contains a comparison between the $\mathcal{L}_2$ cost function results and the predictor alone. The new results are much better in the region near the
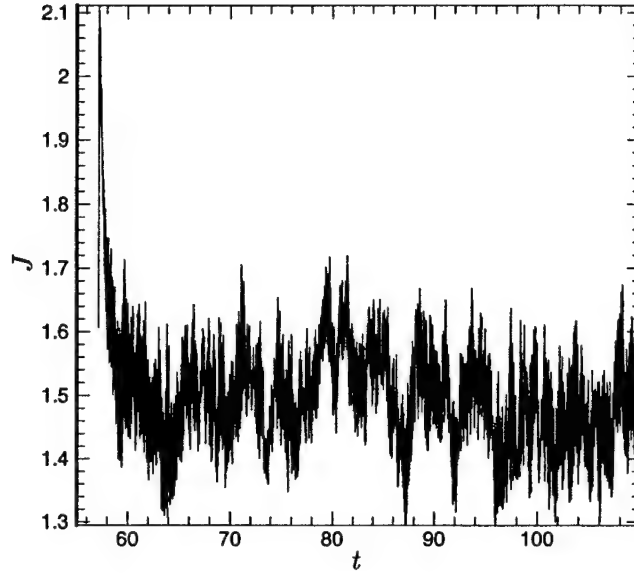
38
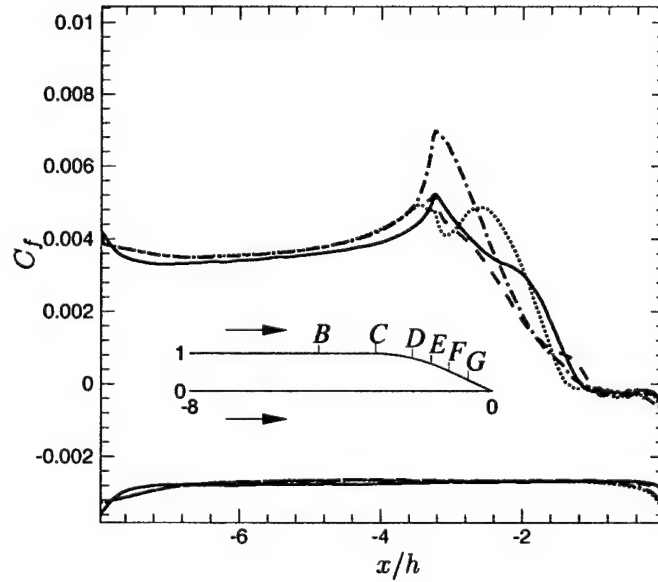
Figure 4.1: $\mathcal{L}_2$ cost function history.

Figure 4.2: Time averaged skin friction over the airfoil surface: ---- , $\mathcal{L}_2$ cost function; —·— , average cost function; ········ , signed cost function; ——— , full LES [41].
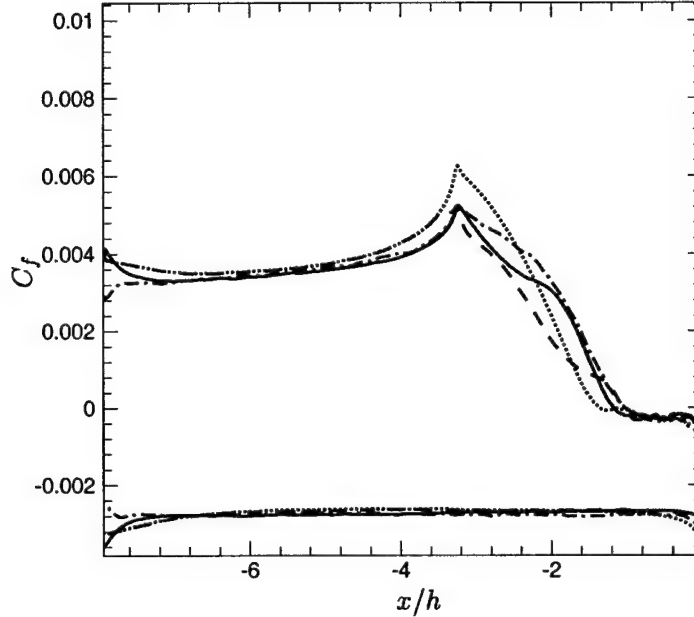
39

Figure 4.3: Time averaged skin friction over the airfoil surface: ‒ ‒ ‒ , $\mathcal{L}_2$ cost function; ⋯⋯ , predictor only; —— , full LES [41]; —·— , TBL equation model [42].

skin friction peak, although they produce a less smooth skin friction profile, and rather large errors remain in part of the adverse pressure gradient region. Overall, the model demonstrates some improvement over the simple wall model used as a predictor, but is less accurate than the full TBL equation model used in [42].

Comparison of the velocities between the full LES and wall modeled LES (based on the $\mathcal{L}_2$ cost function, which produced the best results) are quite good. As shown in Figure 4.4, the coarse grid LES is able to match the resolved LES very closely. The main (moderate) discrepancy occurs in the turbulent intensities near the wall. This is not unreasonable since these quantities were not included in the cost function and it may in fact not be possible to capture these regions accurately because the LES grid does not resolve the intensity peak. When compared to the results of [42] using only the predictor, the results are found to be comparable and in fact are worse for the two cost functions not shown. Therefore, it is difficult to draw definitive conclusions about the effect of the gradient based optimization procedure on the velocity field.

4.4 Channel flow analysis

In order to evaluate the proposed wall model in a more controlled environment, the algorithm has been implemented in the plane channel LES described in Chapter 3. This is a simpler and well known case, so the model can be more readily analyzed. It was immediately noticed that, unlike the trailing edge case, the cost function gradients could not be made independent of the small parameter ϵ used in the finite-difference computation. The gradients monotonically decreased with ϵ until they reached a value of zero. This result indicated that the incomplete sensitivity approach did not accurately capture the gradients in the channel, since non-zero gradients were observed in
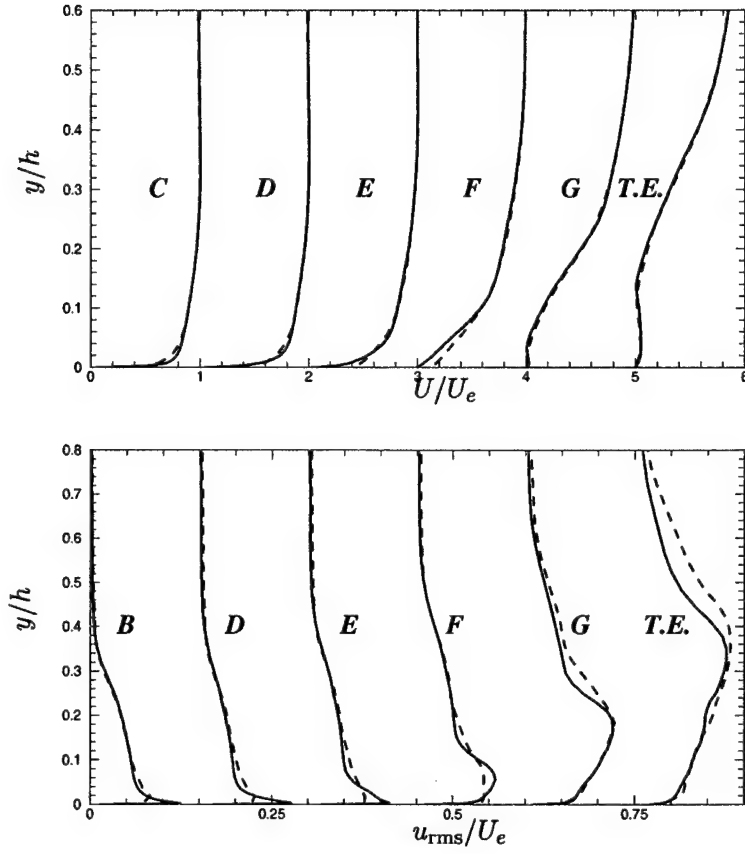
Figure 4.4: Mean velocity magnitude profiles (upper figure) and streamwise component of turbulence intensities (lower figure) at several trailing edge stations: ---- , $\mathcal{L}_2$ cost function; ——— , full LES [41]. Locations are those indicated in Figure 4.2. T.E. is the trailing edge point.

41

the sub-optimally controlled channel. The following analysis is used to explain these results, as well as the difficulties encountered with this method in the trailing edge geometry.

Consider a cost function of form

$$J(a) = \int_S f(u(a))dS. \tag{4.11}$$

Since in the current framework, the shape and shape deformations are defined in two dimensions, the surface can be parameterized by taking the y coordinates as a function of x, i.e. $y = g(x)$. Then the cost function becomes

$$J(a) = \int_0^l f(u(x;a))\sqrt{1 + g'^2(x)}dx. \tag{4.12}$$

Consider a perturbation to this surface parameterized by $\epsilon h(x)$. In the current context, $h(x)$ would correspond to the spline and ϵ to the small change in the control parameter. The new cost function is computed by considering its sensitivity to geometry only, so

$$J(a + \epsilon) = \int_0^l f(u(x;a))\sqrt{1 + (g'(x) + \epsilon h'(x))^2}dx. \tag{4.13}$$

By using a Taylor series expansion, one obtains to $O(\epsilon)$:

$$\sqrt{1 + (g'(x) + \epsilon h'(x))^2} \approx \sqrt{1 + g'^2(x)} + \epsilon(1 + g'^2(x))^{-1/2}g'(x)h'(x). \tag{4.14}$$

When the gradient is computed by taking $(J(a + \epsilon) - J(a))/\epsilon$, the resulting term is

$$\frac{\partial J}{\partial a} \approx \int_0^l f(u(x;a))(1 + g'^2(x))^{-1/2}g'(x)h'(x)dx. \tag{4.15}$$

This expression explains the observed cost function gradients. First, it has been demonstrated in both the trailing edge and channel flows that in regions where the surface is flat, the gradients are zero. This is clear since in these regions, $g'(x) = 0$. A similar observation occurs in areas where the surface is a straight line. This is because $g'(x)$ is constant and, in this case, $h(x)$ is symmetric, meaning that whenever $h'(x) > 0$, there is a corresponding x_1 such that $h'(x_1) = -h'(x)$. Thus, unless $f(u(x;a))$ has a very large change between x and x_1, since $g'(x)h'(x) + g'(x_1)h'(x_1) = 0$ the gradient will be very small.

Finally, it has been observed that in regions of curvature away from the direction of perturbation and for a positive definite $f(u(x;a))$ (such as the $\mathcal{L}_2$ cost function), the gradient is always positive. This can be seen by examining the product $g'(x)h'(x)$. In these regions, $g'(x)$ is always negative and increases monotonically in magnitude. By the symmetry of $h(x)$, the regions where $h'(x)$ is positive correspond to $g'(x)$ having a smaller magnitude, and the regions where $h'(x)$ is negative correspond to $g'(x)$ having a greater magnitude. Thus, the positive contribution is greater in magnitude than the negative contribution, and hence the gradient is positive since $f(u(x;a))$ is positive and varies less than the curvature.

The sensitivity computed by this method is then almost exclusively dependent on the curvature of the function whose information is contained in $g'(x)$. It is difficult to determine how this information could be useful in changing the state u such that the given cost function is minimized in a rigorous and well defined manner. For any cost function defined as above, the incomplete sensitivity method will act in a way directly related to the curvature of the surface. If a correlation exists between reducing this curvature and reducing the cost function, the method may produce reasonable results. However, there is no reason to believe that, in general, reducing surface curvature will be helpful in wall modeling. In fact, as experience in the channel has demonstrated, a region of no curvature still requires control to obtain an accurate solution. Therefore, it is likely that an alternative method must be found for the general application of a wall model.

42

4.5 Conclusions and future work

Wall modeling using control theory is a promising new approach for developing robust wall models which account for not only the unresolved flow physics but also numerical and SGS modeling errors. In this chapter, a methodology has been proposed to overcome the deficiencies of the model by Nicoud *et al.* [33], described in Chapter 3, and make the control-based wall model predictive and practical in terms of computational expense. Two critical components, namely the use of RANS velocity profiles as the near-wall LES target in the cost function and the incomplete sensitivity method for gradient evaluation have been examined and tested in a turbulent trailing edge flow.

Based on the test results, it is clear that the assumption of incomplete sensitivities is not appropriate for LES wall models with the type of cost function considered in this work. This is at least partly due to the cost function measuring the LES state in the flow and not at the wall. A cost function that is more sensitive to the geometry could be better suited, but it is unclear how to formulate such a cost function for a wall model. Furthermore, there is evidence suggesting that in applications similar to this, the gradient calculated with incomplete sensitivities may have not only incorrect magnitude but also incorrect sign [26]. Clearly, a more accurate means is needed to compute the gradient.

The use of a cost function matching a RANS profile near the wall may however prove useful in LES wall modeling. It has a solid physical basis, although the RANS model used here is rather rudimentary. More robust RANS models, such the k-ω model are being considered. In addition to choosing an appropriate RANS model, the choice of matching quantities is also an important factor in the performance of the model. Matching LES and RANS velocities may prove not to be the best quantity to minimize for optimal performance of the model. Cost functions based on vorticity or energy could better account for dynamics that are more important to the large scales in the LES. An investigation of these cost functions and implementation of a RANS model is underway in a channel flow.

Acknowledgments

Bibliography

[1] F. Abergel and R. Temam. On some control problems in fluid mechanics. *Theor. Comput. Fluid Dyn.*, 1:303–325, 1990.

[2] E. Achenbach. Distribution of local pressure and skin friction around a circular cylinder in cross-flow up to $Re = 5 \times 10^6$. *J. Fluid Mech.*, 34:625–639, 1968.

[3] R.J. Adrian, B.G. Jones, M.K. Chung, Y. Hassan, C.K. Nithianandan, and A. Tung. Approximation of turbulent conditional averages by stochastic estimation. *Phys. Fluids A*, 1:992–998, 1989.

[4] J.S. Baggett, J. Jimenez, and A.G. Kravchenko. Resolution requirements in large-eddy simulation of shear flows. *Annual Research Briefs*, Center for Turbulence Research, NASA Ames/Stanford Univ., pp. 51–66, 1997.

[5] J.S. Baggett, F. Nicoud, B. Mohammadi, T. Bewley, J. Gullbrand, and O. Botella. Sub-optimal control based wall models for LES - including transpiration velocity. *Proc. Summer Program*, Center for Turbulence Research, NASA Ames/Stanford Univ., pp. 331–342, 2000.

[6] T.G. Bagwell. *Stochastic Estimation of Near-Wall Closure in Turbulence Models*. PhD thesis, University of Illinois at Urbana-Champaign, 1994.

[7] T.G. Bagwell, R.J. Adrian, R.D. Moser, and J. Kim. Improved approximation of wall shear stress boundary conditions for large eddy simulation. in *Near-Wall Turbulent Flows*, edited by R.M.C. So, C.G. Speziale and B.E. Launder, Elsevier Science, New York, pp. 265–275, 1993.

[8] E. Balaras, C. Benocci, and U. Piomelli. Two-layer approximate boundary conditions for large-eddy simulations. *AIAA Jounal*, 34:1111–1119, 1996.

[9] T. Bewley, H. Choi, R. Temam, and P. Moin. Optimal feedback control of turbulent channel flow. *Annual Research Briefs*, Center for Turbulence Research, NASA Ames/Stanford Univ., pp. 3–14, 1993.

[10] T.R. Bewley. Flow control: new challenges for a new renaissance. *Progress in Aerospace Sciences*, 37:21–58, 2001.

[11] M. Breuer. A challenging test case for large eddy simulation: high Reynolds number circular cylinder flow. *Int. J. Heat Fluid Flow*, 21:648–654, 2000.

[12] W. Cabot. Near-wall models in large-eddy simulations of flow behind a backwards facing step. *Annual Research Briefs*, Center for Turbulence Research, NASA Ames/Stanford Univ., pp. 199–210, 1996.

[13] W. Cabot and P. Moin. Approximate wall boundary conditions in the large-eddy simulation of high Reynolds number flow. *Flow Turb. Combust.*, 63:269–291, 1999.

[14] Y. Chang and S.S. Collis. Active control of turbulent channel flows based on large-eddy simulation. *ASME Paper No. FEDSM-99-6929*, 1999.

[15] H. Choi, R. Temam, P. Moin, and J. Kim. Feedback control for unsteady flow and its application to the stochastic burgers equation. *J. Fluid Mech.*, 253:509–543, 1993.

[16] J.W. Deardorff. Numerical study of three dimensional turbulent channel flow at large Reynolds numbers. *J. Fluid Mech.*, 41:453–480, 1970.

[17] M. Germano. A dynamic subgrid-scale eddy viscosity model. *Phys. Fluids A*, 3:1760–1765, 1991.

[18] G. Grötzbach. Direct numerical and large eddy simulation of turbulent channel flows. in *Encyclopedia of Fluid Mechanics*, edited by N.P. Cheremisinoff, Gulf Publ., West Orange, NJ, pp. 1337–1391, 1987.

[19] F.H. Harlow and J.E. Welch. Numerical calculation of time-dependent viscous incompressible flow of fluid with free surface. *Phys. Fluids*, 8:2182–2189, 1965.

[20] G. Hoffman and C. Benocci. Approximate wall boundary conditions for large eddy simulations. in *Advances in Turbulence V*, edited by R. Benzi, Kluwer, Berlin, pp. 222–228, 1995.

[21] J. Jimenez and R.D. Moser. LES: where we are and what we can expect. *AIAA J.*, 38:605–612, 2000.

[22] J. Kim, P. Moin, and R. Moser. Turbulence statistics in fully developed channel flow at low Reynolds number. *J. Fluid Mech.*, 177:133–166, 1987.

[23] A.G. Kravchenko and P. Moin. Numerical studies of flow over a circular cylinder at $Re_D = 3900$. *Phys. Fluids*, 12:403–417, 2000.

[24] A.G. Kravchenko, P. Moin, and R. Moser. Zonal embedded grids for numerical simulations of wall-bounded turbulent flows. *J. Comp. Phys.*, 127:412–423, 1996.

[25] D.K. Lilly. A proposed modification of the germano subgrid scale closure method. *Phys. Fluids A*, 4:633–635, 1992.

[26] A.L. Marsden, M. Wang, B. Mohammadi, and P. Moin. Shape optimization for trailing-edge noise control. Workshop on Geometry, Dynamics and Mechanics in Honour of the 60th Birthday of J.E. Marsden. Toronto, Canada, August 7, 2002.

[27] P.J. Mason and N.S. Callen. On the magnitude of the subgrid-scale eddy coefficient in large-eddy simulations of turbulent channel flow. *J. Fluid Mech.*, 162:439–462, 1986.

[28] R. Mittal and P. Moin. Suitability of upwind-biased finite difference schemes for large-eddy simulation of turbulence flows. *AIAA J.*, 35:1415–1417, 1997.

[29] B. Mohammadi. Dynamical approaches and incomplete gradients for shape optimization. *AIAA Paper 99-3374*, 1999.

[30] B. Mohammadi, J.I. Moldho, and J. Santiago. Design of minimal dispersion fluidic channels in a cad-free framework. *Proc. Summer Program*, Center for Turbulence Research, NASA Ames/Stanford Univ., pp. 49–62, 2000.

[31] B. Mohammadi and O. Pironneau. *Applied Shape Optimization for Fluids*. Oxford University Press, Oxford, 2001.

[32] F. Nicoud and J.S. Baggett. On the use of optimal control theory for deriving wall models for LES. *Annual Research Briefs*, Center for Turbulence Research, NASA Ames/Stanford Univ., pp. 329–341, 1999.

[33] F. Nicoud, J.S. Baggett, P. Moin, and W. Cabot. Large eddy simulation wall-modeling based on suboptimal control theory and linear stochastic estimation. *Phys. Fluids*, 13:2968–2984, 2001.

[34] A. Papoulis. *Probablility, Random Variables, and Stochastic Processes*. McGraw-Hill, New York, 1965.

[35] U. Piomelli and E. Balaras. Wall-layer models for large-eddy simulations. *Ann. Rev. Fluid Mech.*, 34:349–374, 2002.

[36] U. Piomelli, J. Ferziger, P. Moin, and J. Kim. New approximate boundary conditions for large eddy simulations of wall bounded flows. *Phys. Fluids A*, 1:1061–1068, 1989.

[37] U. Schumann. Subgrid-scale model for finite difference simulations of turbulent flows in plane channels and annuli. *J. Comp. Phys.*, 18:376–404, 1975.

[38] W.C.L. Shih, C. Wang, D. Coles, and A. Roshko. Experiments on flow past rough circular cylinders at large Reynolds numbers. *J. Wind Eng. and Industrial Aerodynamics*, 49:351–368, 1993.

[39] A. Travin, M. Shur, M. Strelets, and P. Spalart. Detached-eddy simulations past a circular cylinder. *Flow Turb. Combust.*, 63:269–291, 1999.

[40] M. Vainberg. *Variational Methods for the Study of Nonlinear Operators*. Holden Day, San Francisco, 1964.

[41] M. Wang and P. Moin. Computation of trailing-edge flow and noise using large-eddy simulation. *AIAA J.*, 38:2201–2209, 2000.

[42] M. Wang and P. Moin. Dynamic wall modeling for large-eddy simulation of complex turbulent flows. *Phys. Fluids*, 14:2043–2051, 2002.

[43] K.A. Warschauer and J.A. Leene. Experiments on mean and fluctuating pressures of circular cylinders at cross flow at very high Reynolds numbers. In *Proc. Int. Conf. on Wind Effects on Buildings and Structures*, Saikon, Tokyo, pp. 305–315, 1971 (see also [45]).

[44] H. Werner and H. Wengle. Large eddy simulation of turbulent flow over and around a cube in a plane channel. In *Selected Papers from the 8th Symposium on Turbulent Shear Flows*, edited by F. Durst, R. Friedrich, B.E. Launder, U. Schumann, and J.H. Whitelaw, Springer, New York, pp. 155–168, 1993.

[45] M.M. Zdravkovich. *Flow Around Circular Cylinders. Vol. 1: Fundamentals*. Oxford University Press, Chap. 6., Oxford, 1997.